JEM Journal of Experimental Medicine

ARTICLE

# Coupling of angiogenesis and odontogenesis orchestrates tooth mineralization in mice

Tomoko Matsubara[1], Takahito Iga[1,2], Yuki Sugiura[3], Dai Kusumoto[4], Tsukasa Sanosaka[5], Ikue Tai-Nagara[1], Norihiko Takeda[6], Guo-Hua Fong[7,8], Kosei Ito[9], Masatsugu Ema[10], Hideyuki Okano[5], Jun Kohyama[5], Makoto Suematsu[3], and Yoshiaki Kubota[1]

**The skeletal system consists of bones and teeth, both of which are hardened via mineralization to support daily physical activity and mastication. The precise mechanism for this process, especially how blood vessels contribute to tissue mineralization, remains incompletely understood. Here, we established an imaging technique to visualize the 3D structure of the tooth vasculature at a single-cell level. Using this technique combined with single-cell RNA sequencing, we identified a unique endothelial subtype specialized to dentinogenesis, a process of tooth mineralization, termed periodontal tip-like endothelial cells. These capillaries exhibit high angiogenic activity and plasticity under the control of odontoblasts; in turn, the capillaries trigger odontoblast maturation. Metabolomic analysis demonstrated that the capillaries perform the phosphate delivery required for dentinogenesis. Taken together, our data identified the fundamental cell-to-cell communications that orchestrate tooth formation, angiogenic–odontogenic coupling, a distinct mechanism compared to the angiogenic–osteogenic coupling in bones. This mechanism contributes to our understanding concerning the functional diversity of organotypic vasculature.**

## Introduction

In vertebrates, the vascular network develops throughout the body to meet tissue demands for oxygen and nutrients and to secrete organotypic paracrine molecules, known as angiocrine factors, that drive cell differentiation and tissue morphogenesis (Potente et al., 2011; Augustin and Koh, 2017; Rafii et al., 2016). Recent advances in histological technology have significantly enhanced our understanding of the spatiotemporal association between angiogenesis and osteogenesis during embryonic and postnatal bone development, particularly in the context of endochondral ossification (Wang et al., 2007; Maes et al., 2010; Kusumbe et al., 2014). The interrelationship between vascular growth and bone formation is known as angiogenic–osteogenic coupling (Maes and Clemens, 2014).

Like bones, teeth are part of the skeletal system. They are essential for daily functions such as mastication and speech. The dental pulp is the anatomically central part of teeth and consists primarily of connective tissues, neurovascular bundles, and odontoblasts, columnar cells lining the surface of the dental pulp (Li et al., 2017; Rombouts et al., 2017; Tucker and Sharpe, 2004). Odontoblasts secrete dentin, a calcified tissue inside the enamel, in the process of dentinogenesis, which is similar to osteoid secretion of osteoblasts during bone development (Thesleff and Sharpe, 1997). Because of the similarity of these processes, the cellular interaction between blood vessels and odontoblasts would reasonably be expected in dentinogenesis, similar to the angiogenic–osteogenic coupling known to occur in bones. However, the tooth is the hardest tissue in the mammalian body, even harder than bones (Simmer et al., 2010). This caveat has hampered precise histological examinations and genetic approaches recently applied to characterize bone angiogenic–osteogenic coupling (Kusumbe et al., 2014, 2015). Therefore, the mechanism and function of angiogenesis in tooth development have thus far remained uncharacterized.

Rodent incisors, which are widely used as an experimental model to study the biology and function of teeth, grow continuously throughout the lifespan, driven by self-renewal of adult stem cells (Kaukua et al., 2014; Biehs et al., 2013). This process does not occur in human teeth. In the present study, to optimize

[1]Department of Anatomy, Keio University School of Medicine, Tokyo, Japan; [2]Department of Orthopedic Surgery, Keio University School of Medicine, Tokyo, Japan; [3]Department of Biochemistry, Keio University School of Medicine, Tokyo, Japan; [4]Department of Cardiology, Keio University School of Medicine, Tokyo, Japan; [5]Department of Physiology, Keio University School of Medicine, Tokyo, Japan; [6]Division of Cardiology and Metabolism, Center for Molecular Medicine, Jichi Medical University, Tochigi, Japan; [7]Center for Vascular Biology, University of Connecticut School of Medicine, Farmington, CT; [8]Department of Cell Biology, University of Connecticut School of Medicine, Farmington, CT; [9]Graduate School of Biomedical Sciences, Nagasaki University, Nagasaki, Japan; [10]Depart of Stem Cells and Human Disease Models, Research Center for Animal Life Science, Shiga University of Medical Science, Shiga, Japan.

Correspondence to Yoshiaki Kubota: ykubo33@a3.keio.jp.

the relevance of mouse studies to the biology of human teeth, we used mouse molars, specifically the first mandibular molar, which lacks adult stem cells and the capacity for renewal after development, similar to human teeth (Tummers and Thesleff, 2003; Li et al., 2015).

Here, to overcome the technical limitations of tooth histology, we first optimized the decalcification solution and processing length before tissue sectioning, and succeeded in visualizing the 3D structure of the tooth vasculature at high resolution. Using this technique in combination with single-cell transcriptomics, we identified that reciprocal feedback between a specialized endothelial population and odontoblasts orchestrates tooth formation.

## Results

### Temporal and spatial characteristics of periodontal tip-like endothelial cells (POTCs)

Initially, we thoroughly optimized the immunohistochemistry protocol, including decalcification time and equipment, ultimately visualizing the 3D structure of the tooth vasculature at high resolution (Fig. 1, A–I). Blood vessels running through the middle of the dental pulp are known to branch from alveolar vessels (Rombouts et al., 2017) and extend small vessels toward the outer surface of the dental pulp, forming a dense capillary plexus (Fig. 1 F). Vascular endothelial growth factor (VEGF) secretion and multiple VEGF receptors are vital for angiogenic processes during development (Potente et al., 2011). Therefore, we examined expression of the VEGF receptors Vegfr1 and Vegfr2 using *Vegfr2-BAC-GFP*$^{+}$*Vegfr1-BAC-DsRed*$^{+}$ mice (Ishitobi et al., 2010; Okabe et al., 2014). In teeth, Vegfr1,2 expression was predominantly localized to endothelial cells (ECs; Fig. 1, E–I). Interestingly, many of the ECs exhibited robust filopodia extensions and concomitantly expressed high levels of Vegfr1 and Vegfr2 (Fig. 1, G–I; and Fig. S1, A–E), in contrast to the side-by-side expression pattern of Vegfr2 and Vegfr1 in endothelial tip and stalk cells of other tissues (Gerhardt et al., 2003; Potente et al., 2011). These capillaries perforated the basal layer of odontoblasts, which was marked by Osterix-positive (Osx$^{+}$) nuclei, thin cytoplasm, and apical processes consisting of an intermediate filament protein, Nestin (Lendahl et al., 1990), whereas in bone tissue, osteoblasts and the vasculature are mutually exclusive (Fig. 1, J–M; and Video 1). These ECs around odontoblasts lacked smooth muscle cells, confirming they indeed formed capillaries (Fig. S1 F). The emergence and expansion of Vegfr1$^{high}$Vegfr2$^{high}$ vasculature occurred at postnatal day 12 (P12), just before the start of mastication and active dentinogenesis (Fig. S1, G–V). Considering these spatial and temporal characteristics, we termed the sprouting Vegfr1$^{high}$Vegfr2$^{high}$ capillaries around odontoblasts POTCs. CD31 was not highly expressed in POTCs (Fig. 1, N–P), unlike type H vessels in developing bones (Kusumbe et al., 2014). Next, we examined the cellular composition of dental pulp and alveolar bone marrow (Fig. 2 A). We detected hematopoietic cells (HCs) and osteoclasts in bone marrow but not in dental pulp (Fig. 2, B–F), suggesting that hematopoiesis and osteoclastogenesis do not occur in the dental pulp.

### POTCs are highly plastic and angiogenic

To evaluate the role of ECs in tooth formation, we targeted their abundant expression of Vegfr1 and Vegfr2 by crossing a tamoxifen-inducible endothelial-specific Cre line, *Cdh5-BAC-Cre*$^{ERT2}$ mice (Okabe et al., 2014), with *Vegfr2-flox* or *Vegfr1-flox* mice, generating endothelial-specific *Vegfr2* and *Vegfr1* knockout mice (*Cdh5–BAC–Cre*$^{ERT2+}$*Vegfr2*$^{flox/flox}$ and *Cdh5–BAC–Cre*$^{ERT2+}$*Vegfr1*$^{flox/flox}$, hereafter referred to as *Vegfr2*$^{i\Delta EC}$ and *Vegfr1*$^{i\Delta EC}$). Stiffness and molar extrusion were reduced in the molars of *Vegfr2*$^{i\Delta EC}$ mice at P12 (Fig. 3, A–C). Consistent with the high dependence of retinal endothelial tip cells on Vegfr2 (Gerhardt et al., 2003), *Vegfr2*$^{i\Delta EC}$ mice exhibited ablated POTCs and endothelial apoptosis, together with decreased odontoblast and dentin widths relative to control mice (Fig. 3, D–S). Conversely, *Vegfr1*$^{i\Delta EC}$ did not manifest detectable defects in gross molar phenotype (Fig. 4, A and B) but did show increased filopodia and vessel areas (Fig. 4, C–J). Mice with combined knockout of *Vegfr1* and *Vegfr2* (*Cdh5–BAC–Cre*$^{ERT2+}$*Vegfr1*$^{flox/flox}$*Vegfr2*$^{flox/flox}$) exhibited ablation of periodontal capillaries and impaired molar formation, similar to *Vegfr2*$^{i\Delta EC}$ mice (Fig. 4, K–N), suggesting that the *Vegfr2* deletion–mediated vascular damage is dominant over hypervascularity caused by *Vegfr1* deletion. The thick vessels in the center of the dental pulp were far less affected in the above mutant mice, suggesting that POTCs were particularly angiogenic and plastic in the tooth vasculature. *Vegfr2*$^{i\Delta EC}$ mice were slightly smaller than control mice at P12, likely reflecting the systemic effect. To mitigate this effect, we conducted a delayed deletion protocol in which 4OHT injection was started at P10 (Fig. S2 A). In this protocol, body length was not affected, but POTC numbers were significantly decreased, and odontoblast maturation and tooth strength were impaired (Fig. S2, B–J). The phenotype in this delayed protocol is likely ascribed to the direct effects of *Vegfr2* deletion on POTCs, although some indirect effects caused by impairment in other vascular beds cannot be excluded definitively.

### Odontoblasts control angiogenic growth of POTCs

In bone development, several cell types, including osteoblasts, hypertrophic chondrocytes, and ECs, contribute to angiogenesis as Vegfa-producing cells (Sivaraj and Adams, 2016). Therefore, we examined *Vegfa* expression in teeth using in situ hybridization, revealing that *Vegfa* was predominantly expressed in odontoblasts (Fig. 5, A–D). *Osx-Cre*$^{ERT2}$ mice, which are widely used to delete genes in osteogenic lineage cells, express Cre in odontoblasts, as demonstrated by crossing with indicator *flox-LSL-GFP* mice (Fig. 5 E). Thus, we generated *Osx-Cre*$^{ERT2}$–specific *Vegfa* knockout mice (*Osx–Cre*$^{ERT2+}$*Vegfa*$^{flox/flox}$). VEGF immunohistochemistry of *Osx-Cre*$^{ERT2+}$*Vegfa*$^{fl/fl}$ mice confirmed that expression of VEGF in osteoblasts was largely diminished (Fig. 5 F). Like *Vegfr2*$^{i\Delta EC}$ mice, *Osx–Cre*$^{ERT2+}$*Vegfa*$^{flox/flox}$ mice exhibited impaired molar extrusion (Fig. 5 G). Histologically, *Osx–Cre*$^{ERT2+}$*Vegfa*$^{flox/flox}$ mice exhibited ablated POTCs and decreased odontoblast and dentin widths (Fig. 5, H–S). These data indicated that odontoblast-derived VEGF is crucial for the growth of POTCs, although a low level of VEGF from other cells expressing *Osx–Cre*$^{ERT2}$ might contribute to the phenotype of *Osx–Cre*$^{ERT2+}$*Vegfa*$^{flox/flox}$ mice. In contrast to osteoblast Vegfr2 expression and function (Hu and Olsen, 2016; Sivaraj and

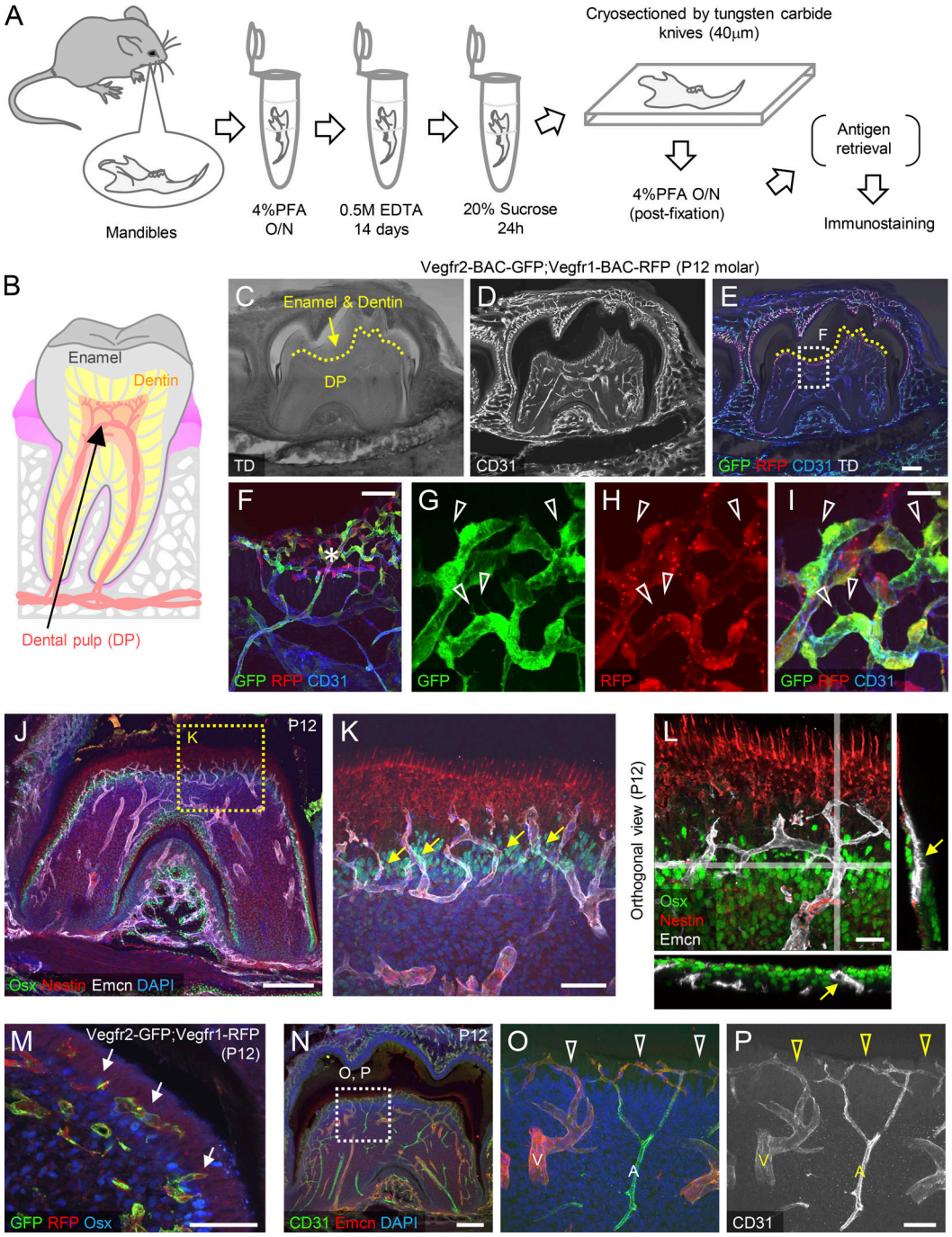


Figure 1. **Temporal and spatial characteristics of POTCs. (A)** Schematic diagram depicting the technique used to visualize tooth vasculature. O/N, overnight. **(B)** Schematic diagram depicting molar structure. **(C–I)** Immunohistochemistry for a mandible centered on the first molar. Dotted lines indicate the border between the dental pulp (DP) and dentin. Many capillary ECs in the periphery (asterisk) were concomitantly Vegfr1$^{high}$ and Vegfr2$^{high}$ and actively sprouting (open arrowheads). **(D)** Fig. S1 I shows the same image for the sake of convenience. **(I)** See also Fig. S1 (A–C) for each channel. **(J–M)** Immunohistochemistry of the first molar at P12. POTCs perforate the basal layer of odontoblasts marked by Osx (arrows). **(N–P)** Immunohistochemistry for the first molar. POTCs (arrowheads) connecting to an arteriole (A) and venule (V) exhibited moderate CD31 intensity. Scale bars: 200 μm (C–E, J, and N); 50 μm (F, K, and M); 20 μm (G–I and L).

Adams, 2016), odontoblast Vegfr2 was dispensable for tooth formation (Fig. S3, A–I).

### Endothelial cells supply phosphate to odontoblasts

Next, we conducted metabolomic analysis of mice to determine how teeth responded metabolically to endothelial *Vegfr2* deletion. Principal component analysis revealed global metabolome changes in *Vegfr2*$^{i\Delta EC}$ mice relative to controls (Fig. 6 A). Volcano plot analysis identified that metabolites related to ketone body metabolism were significantly increased in *Vegfr2*$^{i\Delta EC}$ mice, while the ATP/ADP ratio and creatine phosphate level were decreased in *Vegfr2*$^{i\Delta EC}$ mice, suggesting a decreased

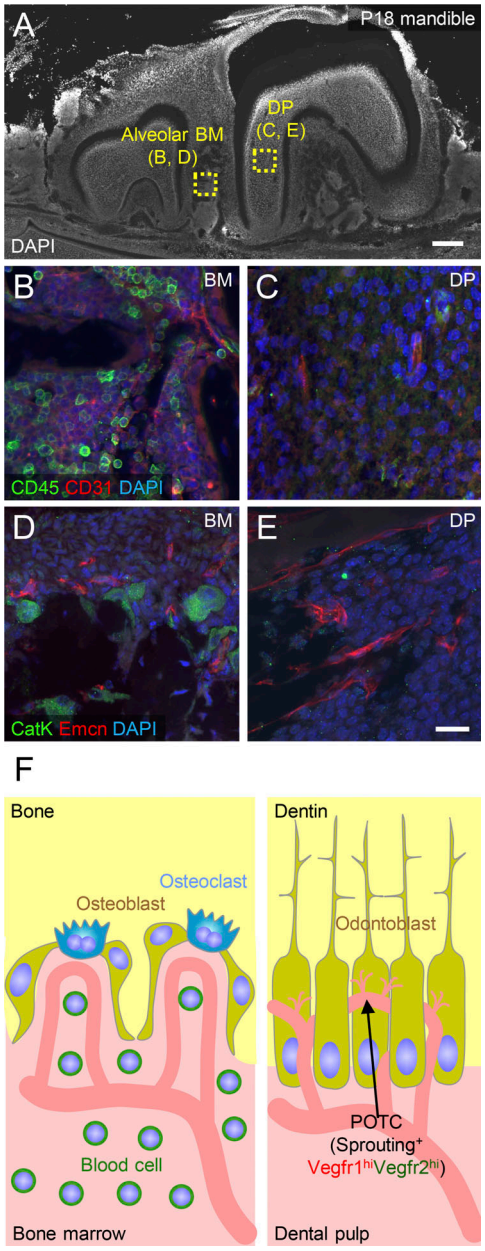


Figure 2. **Hematopoiesis and osteoclastogenesis do not occur in the dental pulp. (A–E)** Immunohistochemistry for a mandible, including first and second molars at P18. CD45+ HCs and CatK+ osteoclasts were detected in the alveolar bone marrow (BM) but not in the dental pulp (DP). **(F)** Schematic diagram depicting the structural and cellular differences between BM and DP. Scale bars: 200 µm (A); 20 µm (B–E).

energy pool and alternatively elevated ketone body metabolism (Fig. 6, B and C; and Table S1). Moreover, tracing intraperitoneally injected stable isotope phosphate ($H_3P[^{18}O]_4$) revealed decreased tissue levels of $H_3P[^{18}O]_4$ (Fig. 6 D), suggesting impaired phosphate delivery in *Vegfr2*$^{i\Delta EC}$ mice. Because phosphate, as well as calcium, are necessary for odontoblasts to mineralize dentin, lack of phosphate transport from ECs could potentially be responsible for impaired tooth formation in *Vegfr2*$^{i\Delta EC}$ mice. Indeed, imaging mass spectrometry (IMS) revealed decreased levels of metabolites associated with the phosphate pathway in *Vegfr2*$^{i\Delta EC}$ mice (Fig. 6 E). Systemic alteration of these metabolites in the circulation, in addition to localized vascular changes, could also contribute to the observed effects in teeth of *Vegfr2*$^{i\Delta EC}$ mice.

### Altered odontoblastic and endothelial heterogeneity in *Vegfr2*$^{i\Delta EC}$ mice

To comprehensively understand the changes in cellular composition and gene expression profile in *Vegfr2*$^{i\Delta EC}$ mice, we conducted single-cell RNA sequencing (scRNA-seq) on cells collected from dental pulps of control and *Vegfr2*$^{i\Delta EC}$ mice (Fig. 7 A and Fig. S4, A and B). Using Uniform Manifold Approximation and Projection (UMAP), we defined 12 cell clusters representing six cell types, including HCs, odontoblasts, myelinated Schwann cells, nonmyelinated Schwann cells, ECs, and mesenchymal stem cells based on known markers (Pagella et al., 2021; Tai-Nagara et al., 2020; Fig. 7, B and C; Fig. S4, C and D; and Table S2). HCs were identified as extravasated macrophages, as immunohistochemistry did not detect rounded myeloid cells (Fig. 2 C). Odontoblasts were divided into one fibroblastic cluster (OB1) and two mature clusters (OB2 and OB3), based on expression of *Fap* (fibroblastic) and *Runx2* (mature) odontoblast markers. Intriguingly, the number of mature odontoblasts was decreased in *Vegfr2*$^{i\Delta EC}$ mice, although the number of fibroblastic cells was increased (Fig. 7 D). A number of genes were affected by *Vegfr2* deletion (Table S3). Gene Ontology (GO) enrichment analysis identified that the biological processes most prominently inhibited in odontoblasts from *Vegfr2*$^{i\Delta EC}$ mice included osteoblast differentiation and ossification, a mineralization process similar to dentinogenesis. Conversely, those enhanced in *Vegfr2*$^{i\Delta EC}$ mice included glycolytic process, blood vessel development, and cellular response to hypoxia (Fig. 7 E and Table S4). A heatmap created by extraction of dentinogenesis genes revealed a broad decrease in *Vegfr2*$^{i\Delta EC}$ mice, especially in OB2, the mature odontoblast cluster (Fig. 7 F). Conversely, Hif-1 target genes, including *Vegfa*, were increased in *Vegfr2*$^{i\Delta EC}$ mice, especially in OB1, the fibroblastic odontoblast cluster (Fig. 7 F). Expression of representative genes for dentinogenesis, including *Dmp1*, *Dspp*, and *Runx2*, was confirmed by quantitative PCR (qPCR) analysis (Fig. S4 E). Reclustering ECs (EC1 and EC2) generated five subclusters, including arterial, venous, capillary endothelial (Capil1 and 2), and POTCs (Fig. 8 A) based on known markers (Vanlandewijck et al., 2018; Kalucka et al., 2020) and expression of *Kdr* (*Vegfr2*) and *Flt1* (*Vegfr1*; Fig. 8 B). Consistent with histological data (Fig. 3, D–G), scRNA-seq analysis confirmed that POTCs were predominantly ablated in *Vegfr2*$^{i\Delta EC}$ mice (Fig. 8 C). Genes known to be enriched in endothelial tip cells (del Toro et al., 2010) were broadly downregulated in ECs of *Vegfr2*$^{i\Delta EC}$ mice (Fig. 8 D and Table S5). Indeed, extraction of differentially expressed genes in POTCs revealed that tip cell genes (*Nid2*, *Esm1*, and *Ramp3*) and Vegf receptors (*Kdr* and *Flt1*) were most strikingly upregulated (Fig. 8 E).

### Angiocrine factors and oxygen regulate odontoblast maturation

The above findings prompted us to determine how ECs support odontoblast maturation and dentinogenesis. As oxygen and

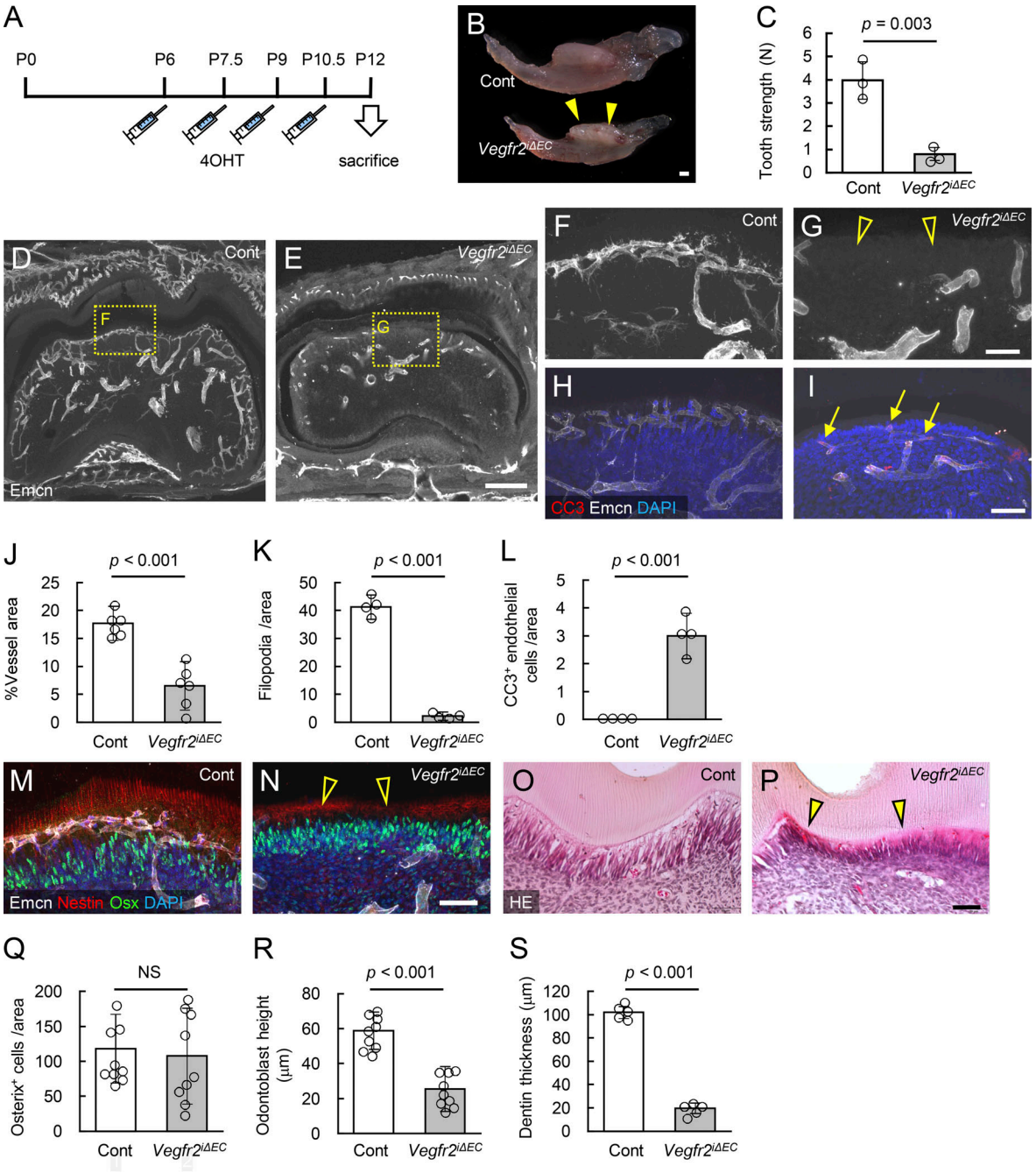


Figure 3. **POTCs grow depending on Vegfr2. (A)** Protocol for 4OHT injection. **(B)** Bright-field view of mandibles. *Vegfr2*$^{i\Delta EC}$ mice exhibited impaired molar extrusions (arrowheads). **(C)** Tooth strength measured by a mechanical testing machine. A load was placed at the center of the molar at a rate of 2 mm/min until the molar broke, and maximum load (N) was measured as tooth strength (control [Cont] $n$ = 3, *Vegfr2*$^{i\Delta EC}$ $n$ = 3). **(D–L)** Section specimens at P12 and quantification (J, Cont $n$ = 6, *Vegfr2*$^{i\Delta EC}$ $n$ = 6; K and L, Cont $n$ = 4, *Vegfr2*$^{i\Delta EC}$ $n$ = 4). *Vegfr2*$^{i\Delta EC}$ mice exhibited decreased POTCs (open arrowheads) associated with apoptosis (arrows), marked by cleaved caspase 3 (CC3). **(M–S)** Section specimens at P12 and quantification (Q and R, Cont $n$ = 9, *Vegfr2*$^{i\Delta EC}$ $n$ = 9; S, Cont $n$ = 5, *Vegfr2*$^{i\Delta EC}$ $n$ = 5). *Vegfr2*$^{i\Delta EC}$ mice exhibited reduction in the height of odontoblasts (open arrowheads). Scale bars: 500 µm (B); 200 µm (D and E); 50 µm (F–I and M–P). Data are presented as means ± SD. Comparisons between two groups were evaluated using a two-sided Student's $t$ test.

nutrients are generally the major effectors provided by blood vessels, we performed organ culture of isolated dental pulps (Fig. 9 A). All of the dentinogenesis markers, including *Dmp1*, *Dspp*, and *Runx2*, were significantly downregulated by hypoxic conditions or serum deprivation (Fig. 9 B). On the other hand, scRNA-seq data identified that paracrine molecules known to promote odontoblast maturation or dentinogenesis, such as *Tgfb1*, *Ptn*, and *Jag2* (Melin et al., 2000; Jin et al., 2021), but not *Vegfa* or *Noggin*, were abundantly expressed in POTCs, which were ablated in *Vegfr2*$^{i\Delta EC}$ mice (Fig. 9 C and Fig. S4 F). To examine the significance of these angiocrine factors, we used the organ culture of dental pulps from *Vegfr2*$^{i\Delta EC}$ mice. Interestingly,

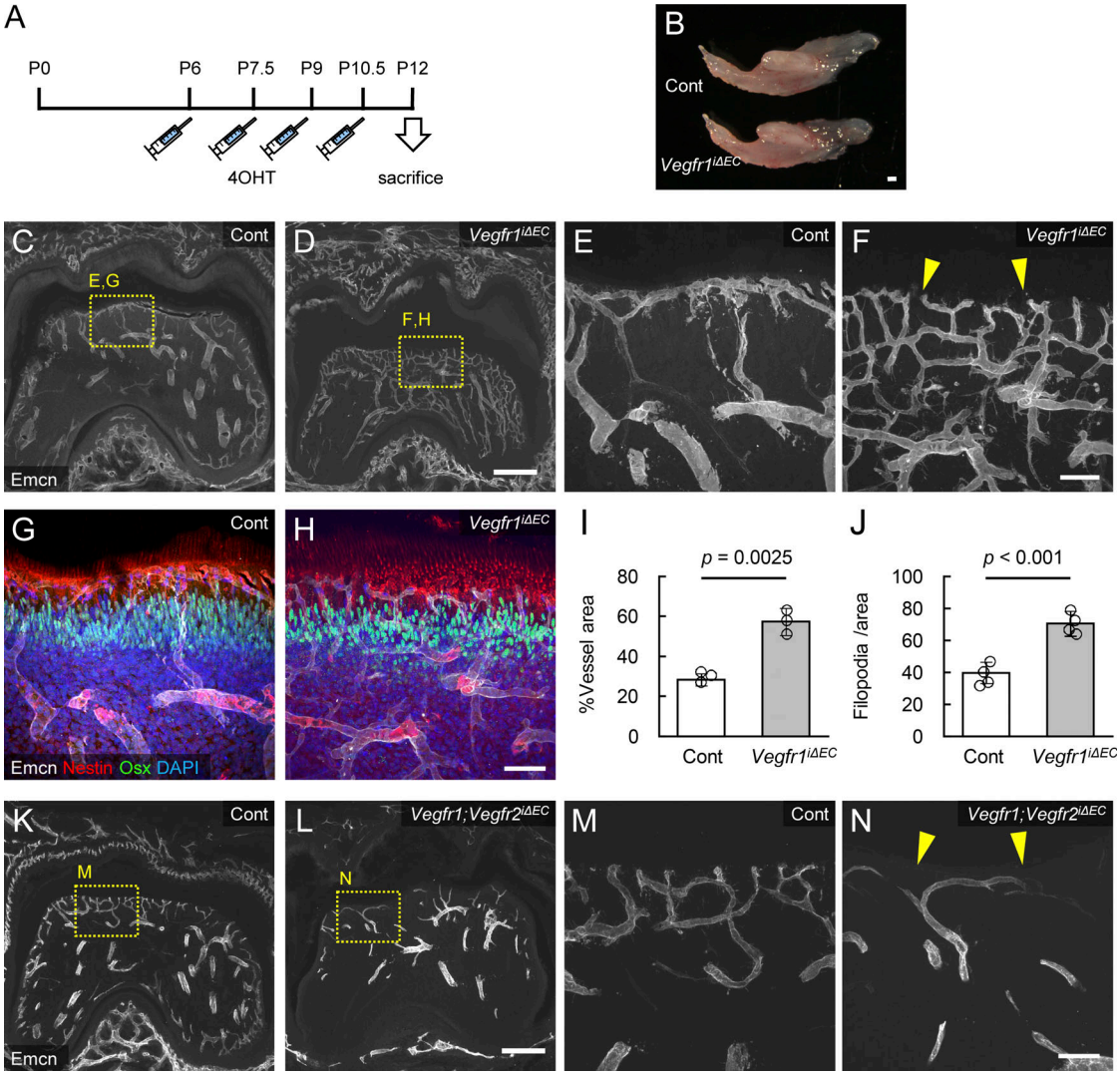


Figure 4. **POTCs overgrow by Vegfr1 deletion. (A)** Protocol for 4OHT injection. **(B)** Bright-field view of mandibles. *Vegfr1*$^{i\Delta EC}$ mice had intact molar extrusion. **(C–J)** Section specimens at P12 and quantification (I, control [Cont] $n$ = 3, *Vegfr1*$^{i\Delta EC}$ $n$ = 3; J, Cont $n$ = 4, *Vegfr1*$^{i\Delta EC}$ $n$ = 4). *Vegfr1*$^{i\Delta EC}$ mice exhibited increased vessel area and filopodia extension (closed arrowheads). **(K–N)** Section specimens at P12. *Vegfr1;Vegfr2*$^{i\Delta EC}$ mice had fewer POTCs (closed arrowheads). Scale bars: 500 µm (B); 200 µm (C, D, K, and L); 50 µm (E–H, M, and N). Data are presented as means ± SD. Comparisons between two groups were evaluated using a two-sided Student's *t* test.

supplementation of recombinant TGFβ and pleiotrophine (PTN) proteins partially, but statistically significantly, restored decreased expression of dentinogenesis markers in dental pulps from *Vegfr2*$^{i\Delta EC}$ mice (Fig. 9 D). To determine which cell types interacted with POTCs, we performed CellPhoneDB analysis (Efremova et al., 2020), a bioinformatics tool that builds cell–cell communication networks using receptor–ligand information. We found that POTCs most abundantly interacted with OB1 and OB2 (Fig. 9 E). Affected ligand–receptor interactions included interactions related to vascular growth and maturation or mineralization of odontoblasts (Fig. 9 F). These data support the idea that not just oxygen and nutrients, but also multiple angiocrine factors, contribute to the regulation of odontoblasts as the effectors of POTCs.

## Discussion

In the present study, we developed a new imaging technique that allowed unprecedented examination of the tooth vasculature. Using multiomics analyses, we identified a reciprocal feedback loop between odontoblasts and a specialized vessel subtype, POTCs, during dental development. In the feedback loop, odontoblasts secrete VEGF to promote angiogenic POTC growth, and POTCs in turn provide odontoblasts with oxygen, phosphate, and odontogenic factors necessary to support their maturation and dentinogenesis. We propose that this interdependent coupling of angiogenesis and odontogenesis could be referred to as "angiogenic–odontogenic coupling," and is a comparable process to angiogenic–osteogenic coupling in bones, although the mechanisms of these two couplings are distinct (Fig. 9 G).

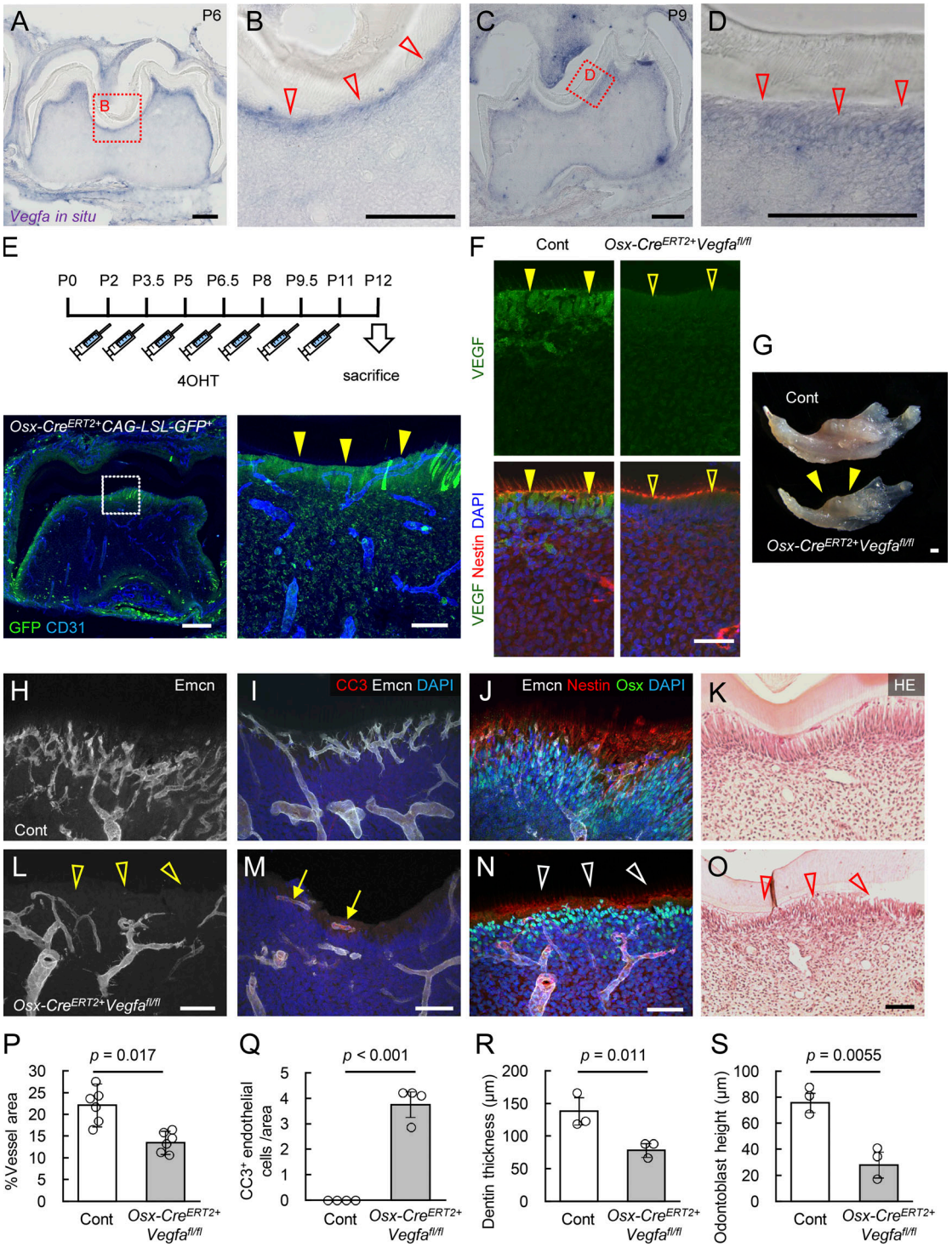


Figure 5. **VEGF-dependent vascular growth promotes dentin secretion from odontoblasts. (A–D)** In situ hybridization of mandibular sections. *Vegfa* mRNA was abundantly expressed in odontoblasts (arrowheads). **(E)** Protocol for 4OHT injection for Cre induction in *Osx-Cre*$^{ERT2}$ mice and immunohistochemistry at P12. Odontoblasts were clearly marked by *Osx-Cre*$^{ERT2}$ (arrowheads). **(F)** Immunohistochemistry at P12. Vegfa expression surrounding odontoblasts observed in control mice (closed arrowheads) is not detectable in *Osx–Cre*$^{ERT2+}$*Vegfa*$^{flox/flox}$ mice (open arrowheads). **(G)** Bright-field view of mandibles. *Osx–Cre*$^{ERT2+}$*Vegfa*$^{flox/flox}$ mice had impaired molar extrusion (arrowheads). **(H–S)** Section specimens at P12 and quantification (P, control [Cont] $n = 6$, *Osx–Cre*$^{ERT2+}$*Vegfa*$^{flox/flox}$ $n = 6$; Q, Cont $n = 4$, *Osx–Cre*$^{ERT2+}$*Vegfa*$^{flox/flox}$ $n = 4$; R and S, Cont $n = 3$, *Vegfr2*$^{i\Delta EC}$ $n = 3$). *Osx–Cre*$^{ERT2+}$*Vegfa*$^{flox/flox}$ mice exhibited decreased POTCs (open arrowheads in L), increased endothelial apoptosis (arrows), and decreased odontoblast height (open arrowheads in N and O). Scale bars: 500 µm (G); 200 µm (A–D and E [left]); 50 µm (E [right], F, and H–O). Data are presented as means ± SD. Comparisons between two groups were evaluated using a two-sided Student's *t* test.

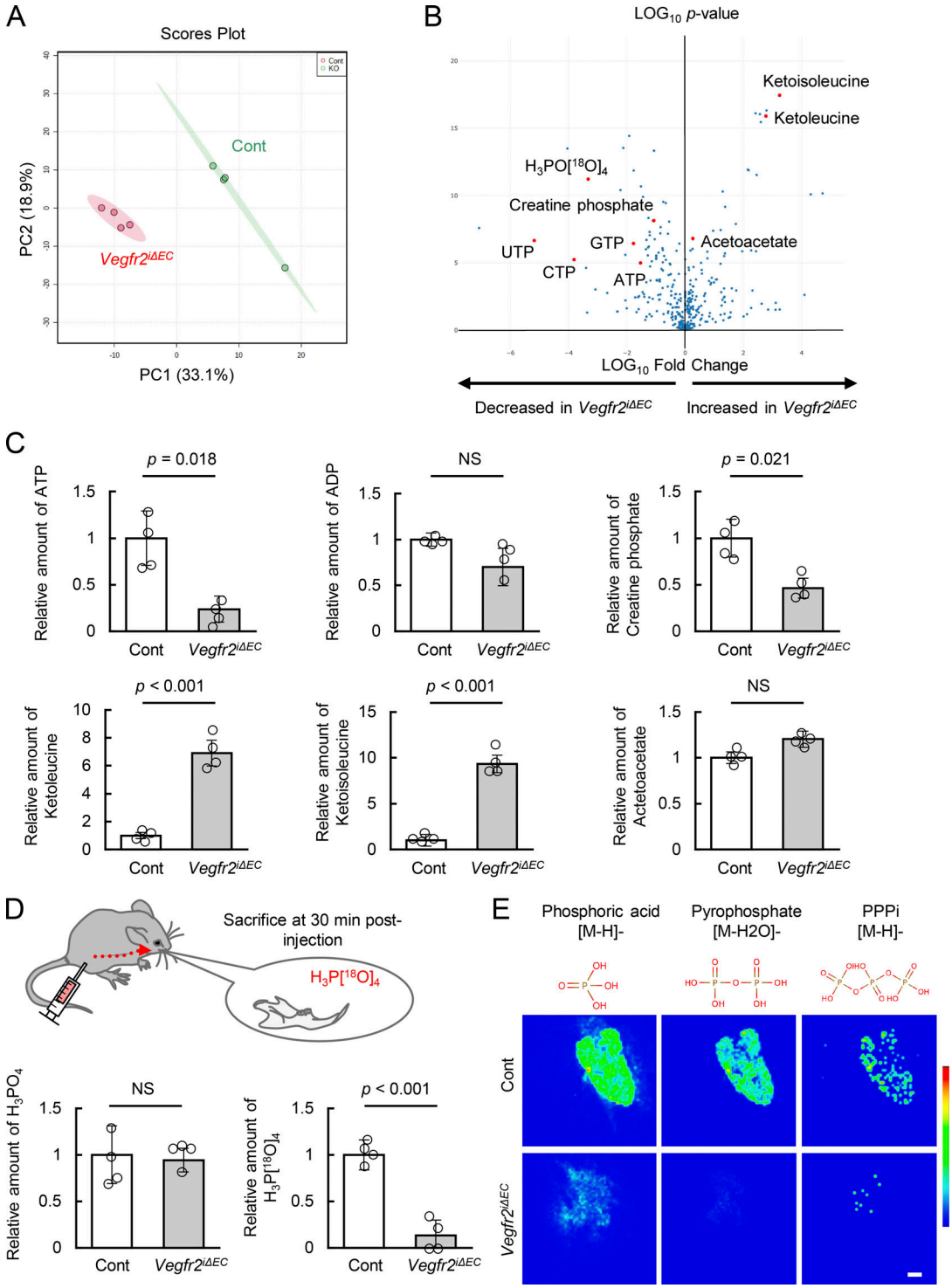


Figure 6. **Endothelial cells supply phosphate to odontoblasts. (A)** Principal component analysis of metabolome profiles of dental pulp samples from control or *Vegfr2*$^{i\Delta EC}$ mice at P12 (control [Cont] $n = 4$, *Vegfr2*$^{i\Delta EC}$ $n = 4$). PC, principal component. **(B)** Volcano plot analysis of metabolites in *Vegfr2*$^{i\Delta EC}$ mice relative to control mice. Red plots represent key metabolites of ketone body metabolism or energy metabolism. Mice were injected with $H_3P[^{18}O]_4$ to trace phosphate delivered by blood vessels. **(C)** Relative intracellular metabolite levels quantified by IC-MS (peak area/internal standard (IS)/tissue-mg; Cont $n = 4$, *Vegfr2*$^{i\Delta EC}$ $n = 4$). **(D)** Relative amounts of $H_3PO_4$ and $H_3PO[^{18}O]_4$ were quantified by IC-MS analysis (Cont $n = 4$, *Vegfr2*$^{i\Delta EC}$ $n = 4$). **(E)** IMS visualizing the amounts and localizations of phosphoric acid, pyrophosphate, and triphosphoric acid (PPPi). Scale bar: 200 µm. Data are presented as means ± SD. Comparisons between two groups were evaluated using a two-sided Student's *t* test.

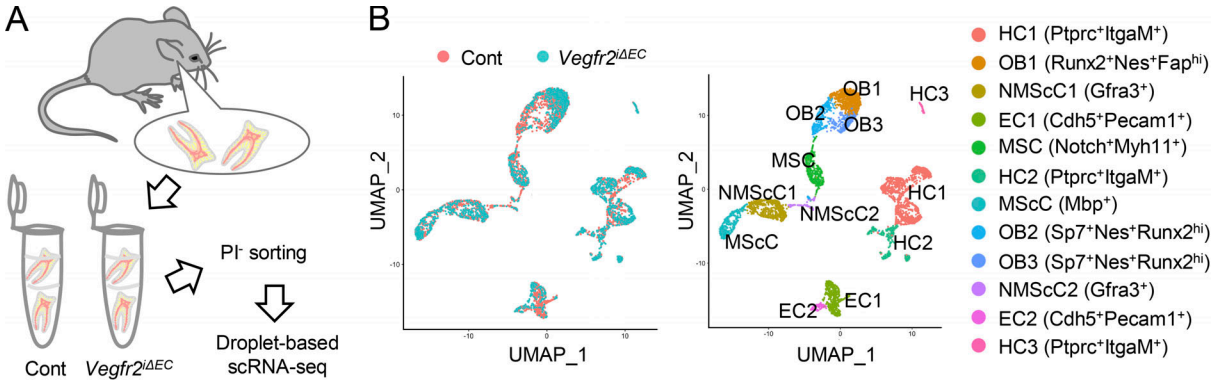


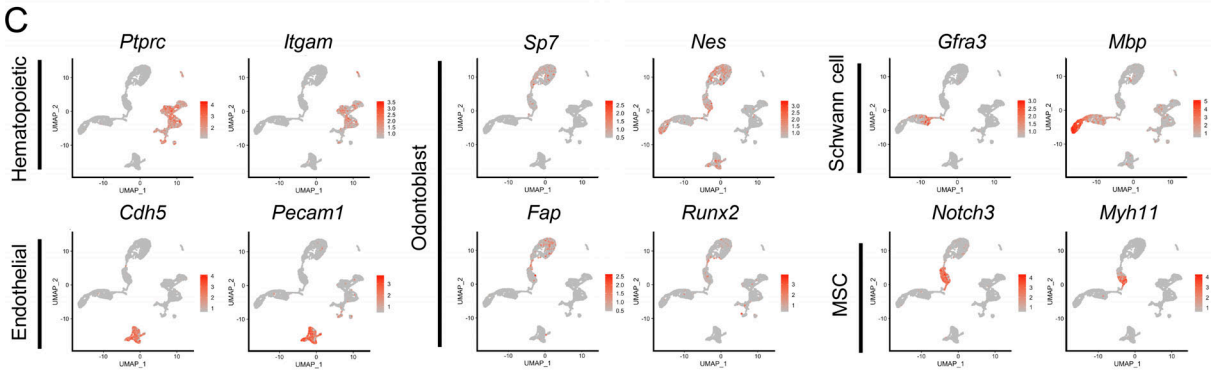


D

| | HC1 | OB1 | NM-ScC1 | EC1 | MSC | HC2 | M-ScC | OB2 | OB3 | NM-ScC2 | EC2 | HC3 |
|---|---|---|---|---|---|---|---|---|---|---|---|---|
| cont | 20.1 | 13.8 | 10.2 | 12.7 | 10.0 | 5.7 | 6.1 | 9.0 | 6.1 | 2.9 | 2.1 | 1.1 |
| *Vegfr2*$^{i\Delta EC}$ | 27.7 | 15.1 | 10.8 | *5.2 | 8.7 | 10.9 | 10.0 | *2.8 | 4.1 | 1.2 | 1.9 | 1.6 |

*FC>2.5

E

Cont>*Vegfr2*$^{i\Delta EC}$

| GO (biological process) | *p*-value |
|---|---|
| translation | 7.01E-27 |
| RNA splicing | 3.68E-07 |
| mRNA processing | 2.95E-06 |
| cytoplasmic translation | 3.49E-06 |
| osteoblast differentiation | 8.47E-05 |
| axonogenesis | 2.21E-03 |
| ossification | 0.0319198 |
| cell migration | 3.26E-02 |

Cont<*Vegfr2*$^{i\Delta EC}$

| GO (biological process) | *p*-value |
|---|---|
| negative regulation of apoptotic process | 7.95E-11 |
| glycolytic process | 6.15E-09 |
| transcription, DNA-templated | 6.01E-07 |
| cell proliferation | 9.56E-06 |
| cell differentiation | 1.15E-05 |
| blood vessel development | 1.72E-05 |
| cellular response to hypoxia | 1.88E-04 |
| gluconeogenesis | 2.09E-04 |

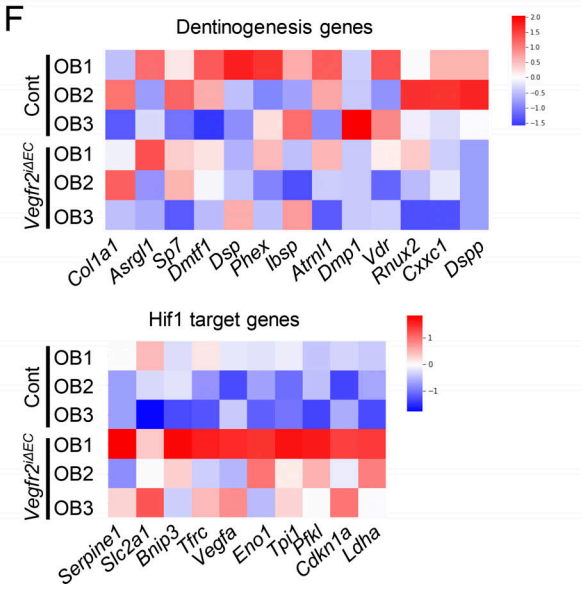


Figure 7. **Altered odontoblastic and endothelial heterogeneity in *Vegfr2*$^{i\Delta EC}$ mice. (A)** Schematic diagram depicting the strategy for scRNA-seq analysis of dental pulp cells. **(B and C)** UMAP plot of cells from control and *Vegfr2*$^{i\Delta EC}$ mice at P12. Clustering was performed based on expression of canonical cell-type markers for HCs (HC1, HC2, and HC3), odontoblasts (OB1 and OB2), myelinated Schwann cells (MScCs), non-myelinated Schwann cells (NMScC1 and NMSsC2), EC1s and EC2s, and mesenchymal stem cells (MSCs). **(D)** Cell counts (%) for each cluster shown in B. Red color indicates FC >2.5. **(E)** Gene ontologies for differentially expressed genes upregulated or downregulated in *Vegfr2*$^{i\Delta EC}$ compared with control mice. Eight representative ontologies sorted from the top 25 ontologies are shown. **(F)** Heatmaps showing expression level of dentinogenesis genes extracted from the gene list GOBP_ODONTOGENESIS_OF_DENTIN_CONTAINING_TOOTH (M15056) or Hif-1 target genes extracted from the list SEMENZA_HIF1_TARGETS (M12299) in the website for gene set enrichment analysis (https://www.gsea-msigdb.org/gsea/msigdb/index.jsp).

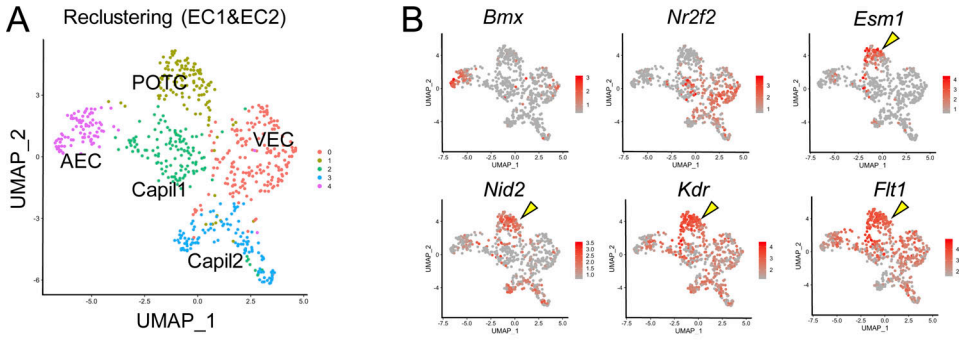


| | VEC | POTC | Capil1 | Capil2 | AEC |
|---|---|---|---|---|---|
| cont | 26.2 | 24.3 | 16.9 | 21.5 | 11.1 |
| *Vegfr2*$^{i\Delta EC}$ | 37.5 | *7.7 | 28.6 | *6.0 | 20.2 |

*FC>2.5

E

Genes upregulated in POTC (vs all ECs)

| Gene | p_val | avg_log2FC |
|---|---|---|
| *Esm1* | 3.52E-48 | 2.38 |
| *Kdr* | 1.39E-41 | 1.51 |
| *Cd300lg* | 7.97E-46 | 1.50 |
| *Ivns1abp* | 3.62E-27 | 1.46 |
| *Col15a1* | 2.26E-38 | 1.40 |
| *Col13a1* | 5.68E-33 | 1.39 |
| *Rgcc* | 3.33E-33 | 1.37 |
| *Plpp3* | 9.77E-31 | 1.36 |
| *Adamtsl2* | 1.89E-61 | 1.35 |
| *Ramp3* | 1.47E-33 | 1.33 |
| *Nid2* | 3.14E-33 | 1.29 |
| *Lamb1* | 1.26E-29 | 1.21 |
| *Flt1* | 9.98E-35 | 1.21 |

Genes upregulated in POTC (vs Capil1)

| Gene | p_val | avg_log2FC |
|---|---|---|
| *Nid2* | 2.18E-25 | 1.34 |
| *Cd300lg* | 2.38E-24 | 1.25 |
| *Kctd12b* | 2.79E-23 | 1.23 |
| *Ecm1* | 1.07E-22 | 0.97 |
| *Adamtsl2* | 1.63E-22 | 0.83 |
| *Myct1* | 1.09E-21 | 1.03 |
| *Prdm1* | 1.49E-21 | 1.02 |
| *Kdr* | 3.88E-21 | 1.31 |
| *Sema7a* | 3.92E-21 | 0.89 |
| *Ndufa13* | 4.75E-21 | 0.74 |
| *Pcdh12* | 1.89E-20 | 0.81 |
| *Esm1* | 2.76E-20 | 1.70 |
| *Ramp3* | 9.82E-20 | 1.25 |

Figure 8. **POTCs were predominantly ablated by Vegfr2 deletion. (A and B)** UMAP plots for reclustered EC1 and EC2 cells in Fig. 7 B. Types of ECs are assigned based on known markers for arterial endothelial cells (AECs), venous endothelial cells (VECs), capillary endothelial cells (Capil1, 2), and POTCs. **(C)** UMAP plots for reclustered EC1 and EC2 cells and cell counts (%) for each cluster. Red color indicates FC >2.5. **(D)** Heatmaps showing expression levels of endothelial tip cell marker genes. **(E)** Top 13 upregulated genes in POTCs (vs. all EC clusters or vs. Capil1). Red color indicates gene markers for tip cells and VEGF receptors.

Interaction between blood vessels and parenchymal cells is essential to ensure the diversity of organotypic vasculature. Therefore, mechanisms of these interactions likely differ depending on the organ. The cell-to-cell interaction observed in teeth is similar to that of the developing retina. Retinal astrocytes in hypoxic regions of the retina secrete VEGF to promote angiogenesis. In turn, newly formed blood vessels provide the oxygen and leukemia inhibitory factor to relieve hypoxia and promote astrocyte maturation (West et al., 2005; Kubota et al., 2008). Future studies will examine the role of hypoxia-inducible factors in odontoblasts in tooth vascular growth.

Together, the teeth and bones comprise the skeletal system, which is mineralized and hardened during development. However, angiogenic–osteogenic coupling in bones differs from angiogenic–odontogenic coupling in teeth. First, in bones, osteoblasts are not the primary source of VEGF, which is instead predominantly expressed by hypertrophic chondrocytes (Gerber et al., 1999; Duan et al., 2015), suggesting that the direct contribution of osteoblasts to angiogenesis is minor compared with the indispensable role of odontoblast-secreted VEGF in tooth angiogenesis and development. It is also noteworthy that VEGF inhibition increased the layer of hypertrophic chondrocytes in

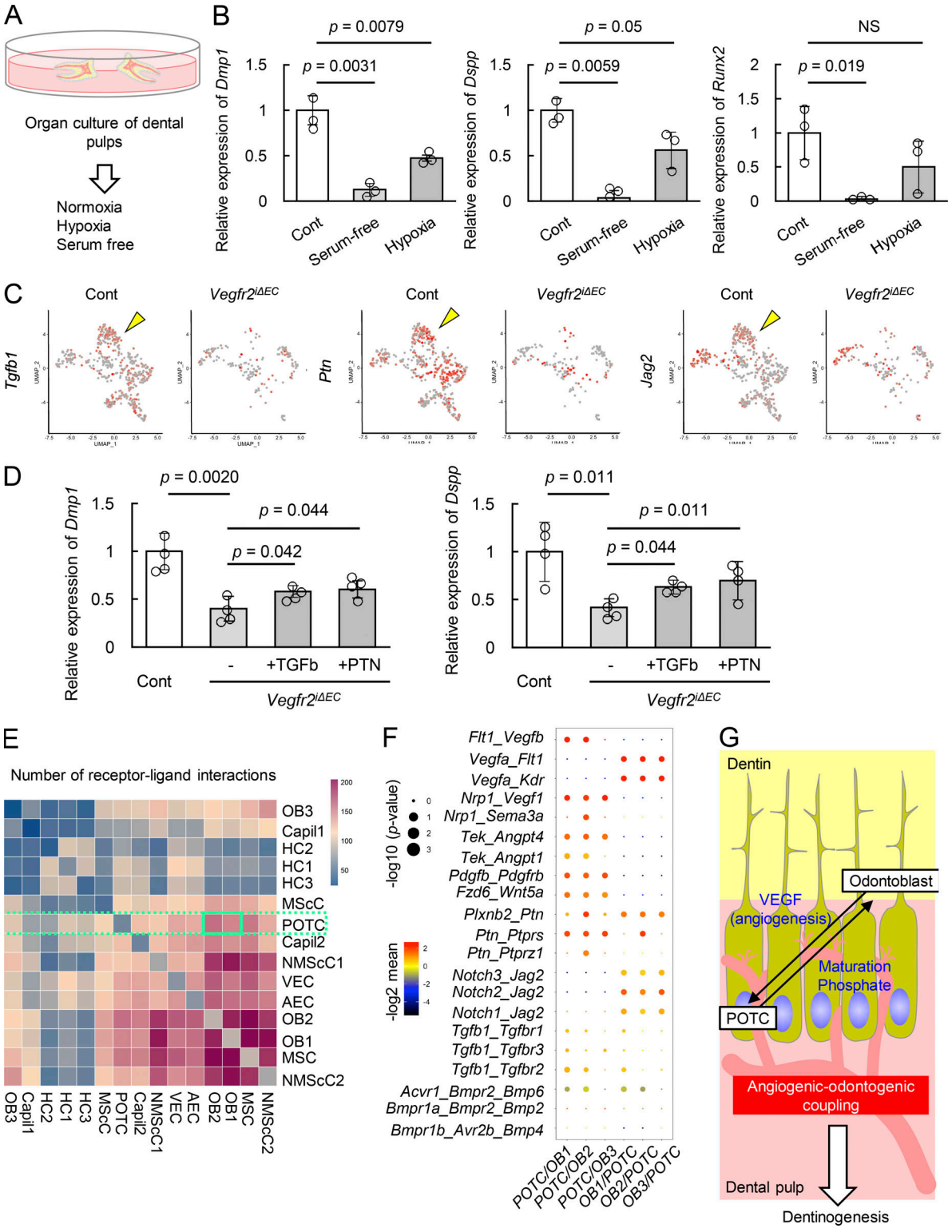


Figure 9. **Angiocrine factors and oxygen regulate odontoblasts maturation. (A)** Schematic diagram depicting the organ culture procedure for dental pulps. **(B)** qPCR analysis for dental pulps cultured for 24 h (control [Cont] $n = 3$, serum-free $n = 3$, hypoxia $n = 3$). **(C)** UMAP plots showing expression of genes known to promote odontoblast maturation. Arrowheads indicate POTCs. **(D)** qPCR analysis for dental pulps cultured for 24 h (Cont $n = 4$, *Vegfr2*$^{i\Delta EC}$ $n = 4$, *Vegfr2*$^{i\Delta EC}$ + Tgfb $n = 4$, *Vegfr2*$^{i\Delta EC}$ + PTN $n = 4$). **(E)** CellPhoneDB analysis predicting intercellular interactions among various cell types in the dental pulp. The number of receptor–ligand interactions for POTCs (dotted square) was highest in OB1 and OB2 cells (solid square). **(F)** Dot plot indicating an array of receptor–ligand couples, with dot color and size representing the strength and significance of the predicted interaction between cell types. **(G)** Schematic diagram depicting the bidirectional interaction between odontoblasts and blood vessels. Data are presented as means ± SD. Comparisons between two groups were evaluated using a two-sided Student's *t* test.

bones (Gerber et al., 1999). The characteristics of the specialized vessel subtypes in bones and teeth also differ. There are two primary vessel populations in bone marrow: type S ($CD31^{low}Emcn^{low}$) and type H ($CD31^{high}Emcn^{high}$). $CD31^{high}Emcn^{high}$ vessels are the primary contributors to osteogenesis (Kusumbe et al., 2014). However, there is no such distinction in teeth. POTCs express CD31 and Emcn at levels similar to other vessels located in the inner portion of the dental pulp. Moreover, the $Vegfr2^{high}Vegfr1^{high}$ feature of POTCs is not present in bone type H vessels in bones (not depicted).

In summary, our findings uncovered a fundamental process of intercellular communication required for tooth development. The concept of angiogenic–odontogenic coupling could contribute to the development of effective regenerative therapies for tooth loss. Moreover, the mechanisms of how blood vessels orchestrate tooth mineralization extend the knowledge base regarding skeletal development and the diversity of organotypic vasculature and angiocrine signaling.

## Materials and methods

### Mice

Animal care was approved by the Institutional Animal Care and Use Committee of Keio University and performed in accordance with the Guidelines of Keio University for Animal and Recombinant DNA Experiments. *CAG-LSL-GFP* (Kawamoto et al., 2000), *Vegfr1-BAC-DsRed*, and *Vegfr2-BAC-GFP* (Ishitobi et al., 2010; Okabe et al., 2014) mice have been described previously. *Cdh-BAC-Cre$^{ERT2}$*mice, which were previously described (Okabe et al., 2014), were crossed with *Vegfr2-flox* mice (Hooper et al., 2009) and *Vegfr1-flox* mice (Ho et al., 2012). *Cdh5-BAC-Cre$^{ERT2}$Vegfr2$^{flox/+}$* and *Cdh5-BAC-Cre$^{ERT2}$Vegfr1$^{flox/+}$* mice were used as littermate controls, respectively. *Osx–Cre$^{ERT2}$* mice (Maes et al., 2010; Ono et al., 2016) were mated with *Vegfa-flox* mice (provided by Genentech; Gerber et al., 1999). The mutant mice were crossed with C57BL/6J mice >10 times. For tamoxifen-inducible animals, 4-hydroxytamoxifen (40 µg) dissolved in oil/EtOH (4:1) at 2 mg/ml was injected s.c. at the indicated time points. For analysis, mice of both sexes were used without exact determination.

### Preparation of mandibular sections

Surgically dissected mandibles were fixed overnight in 4% paraformaldehyde in PBS. For decalcification, samples were immersed in 0.5 M EDTA for 7 d at P6, 14 d at P12, and 28 d at P18 and P24. Samples were carefully embedded in optimum cutting temperature compound under a microscope to ensure that sectional planes were parallel and were then cryosectioned at 40-µm thickness (HM550; Thermo Fisher Scientific) using tungsten carbide knives (Thermo Fisher Scientific). All sections were stained as described below.

### Immunostaining and in situ hybridization

Immunohistochemistry of whole-mount samples or tissue sections was performed as described previously (Kubota et al., 2011). The primary monoclonal antibodies used were hamster anti-CD31 (MAB1398Z; 1:1,000; Chemicon), Nestin (Rat401; 1:200; BD Pharmingen), VEGFR2 (Avas12a1; 1:200; BD Pharmingen), and CD45 (30-F11; 1:500; BD Pharmingen). The primary polyclonal antibodies used were Alexa Fluor 488–conjugated anti-GFP (A21311; 1:500; Molecular Probes), Endomucin (sc-65495; 1:500; Santa Cruz), Osterix (ab22552; 1:500; Abcam), Cathepsin K (ab19027; 1:500; Abcam), and cleaved caspase 3 (9694; 1:200; Cell Signaling). Secondary antibodies used were Alexa Fluor 488–conjugated IgGs (A11034, A11006, A11055; 1:500; Molecular Probes) or Cy3/Cy5 DyLight549/DyeLight649-conjugated IgGs (711-165-152, 112-165-167, 127-165-160, 711-605-152, 112-605-167, 127-605-160; 1:500; Jackson ImmunoResearch). For nuclear staining, specimens were treated with DAPI (D-1306; Molecular Probes). For in situ hybridization, mandibular sections generated in RNAse-free conditions were hybridized with digoxigenin-labeled antisense RNA probes, as described previously (Kubota et al., 2011).

### Confocal microscopy

Fluorescent images were obtained using a confocal laser scanning microscope (FV3000; Olympus). Imaris software (Bitplane) was used to obtain orthogonal views and create a 3D video from multislice Z-stack images. Quantification of dentin thickness and odontoblast height was measured at the maximal points in the tooth sections. Measurement of vessel area, filopodia number, and $Osx^+$ cells was conducted in 300 × 300-µm fields of view in each sample using the FV10-ASW 3.0 Viewer (Olympus) and ImageJ software (National Institutes of Health).

### Dental pulp culture

Dental pulps were isolated en bloc from first molars removed from the mandibles and then thoroughly washed with PBS. Thereafter, the isolated whole-mount dental pulps were transferred into 1 ml DMEM (Sigma-Aldrich), with or without 10% FBS, and cultured in 96-well culture plates (Corning) at 37°C in 20% (normoxic) or 1% (hypoxic) $O_2$ for 24 h. In some experiments, recombinant human PTN (1 µg/ml; R&D Systems) or 20 ng/ml human TGFβ (Abcam) proteins were added to culture medium.

### Cell isolation using Dynabeads

Dental pulps were incubated for 30 min at 37°C in DMEM containing 1% collagenase D (from *Clostridium histolyticum*; Sigma-Aldrich), 1 U/ml dispase (Thermo Fisher Scientific), and 1 U/ml DNase (Invitrogen) before cells were dissociated by gentle trituration. Cells were isolated using Dynabeads (Veritas), according to the manufacturer's instructions. To isolate ECs, cells were incubated with an anti-CD31 antibody (BD Biosciences) preconjugated to Dynabeads (M-450) anti-Rat IgG, and positively selected as $CD31^+$ cells.

### qPCR analysis

Total RNA was prepared from fresh or cultured dental pulps, and reverse transcription was performed using Superscript III (Invitrogen). qPCR assays were performed with the ABI 7500 Fast Real-Time PCR System using TaqMan Fast Universal PCR Master Mix (Applied Biosystems) and TaqMan Gene Expression Assay Mix with *Dmp1* (Mm00803833_g1), *Dspp* (Mm00515666_m1), *Runx2* (Mm00501578_m1), *Col1a1* (Mm01302043_g1), *Vegfr1*

(Mm00438780_m1), and *Vegfr2* (Mm00440099_m1). A mouse *β-actin* (Mm00607939_s1) assay mix served as an endogenous control. Data were analyzed using 7500 Fast System SDS Software 1.3.1.

### Sample preparation for $^{18}O$ metabolic pathway tracing analysis

To analyze metabolic pathways in dental pulp cells, $H_3PO_4[^{18}O]_4$ (1 mg/body weight [g]; Taiyo Nissan) was intraperitoneally injected 30 min before sacrificing pups. Dissected dental pulps were immediately frozen and stored at −80°C until use. Tissues were used for both metabolomic analysis and IMS. Metabolite extraction for metabolomics was performed as described previously (Sugiura et al., 2014; Yamamoto et al., 2014; Morita et al., 2018). Briefly, frozen tissue blocks, together with internal control compounds (2-morpholinoethanesulfonic acid), were homogenized in ice-cold methanol (500 µl) using a manual homogenizer (Finger Masher [AM79330]; Sarstedt), followed by addition of an equal volume of chloroform and 0.4 times the volume of ultrapure water (LC/MS grade; Wako). The suspension was then centrifuged at 15,000 *g* for 15 min at 4°C. After centrifugation, the aqueous phase was filtered using an ultrafiltration tube (Ultrafree-MC; UFC3 LCC NB; Human Metabolome Technologies). The filtrate was concentrated with a vacuum concentrator (SpeedVac; Thermo Fisher Scientific). The concentrated filtrate was dissolved in 50 µl ultrapure water and used for metabolomic analysis. $H_3PO_4$ and $H_3P[^{18}O]_4$ levels were measured as described below.

### Metabolome analysis

For metabolomic analysis of central glucose metabolic pathways, including glycolysis, the TCA cycle, and the pentose phosphate pathway, anion metabolites were measured using an orbitrap-type mass spectrometer (MS; Q-Exactive Focus; Thermo Fisher Scientific) connected to a high-performance ion chromatography (IC) system (ICS-5000+; Thermo Fisher Scientific), enabling us to perform highly selective and sensitive metabolite quantification owing to the IC separation and Fourier transfer MS principle (Hu et al., 2015). We note that IC can measure not only organic compounds, but also inorganic phosphoric acids. The IC device was equipped with an anion electrolytic suppressor (Dionex AERS 500; Thermo Fisher Scientific) to convert the potassium hydroxide gradient into pure water before the sample entered the MS. The separation was performed using a Dionex IonPac AS11-HC, 4-µm-particle-size column (Thermo Fisher Scientific). The IC flow rate was 0.25 ml/min, supplemented postcolumn with a 0.18-ml/min methanol makeup flow. The potassium hydroxide gradient conditions for IC separation were 1–100 mM for 0–40 min, 100 mM for 40–50 min, and 1 mM for 50.1–60 min at a column temperature of 30°C.

### Matrix-assisted laser desorption/ionization (MALDI)–IMS

MALDI imaging analyses were performed as described previously (Sugiura et al., 2016). Briefly, thin sections (8 µm) were prepared using a cryomicrotome (CM3050; Leica Microsystems). Sections were attached to indium tin oxide–coated glass slides (Bruker Daltonics) and coated with 9-aminoacridine as a matrix (10 mg/ml, dissolved in 80% ethanol) by manually spraying with an artist brush (Procon Boy FWA Platinum; Mr. Hobby). MALDI imaging was performed using an orbitrap MS (QExactive Focus; Thermo Fisher Scientific) coupled with an atmospheric pressure scanning microprobe MALDI ion source (AP-SMALDI10; TransMIT). For the orbitrap MS, signals within a mass range 50–400 were acquired with a mass resolving power of 70,000 at *m/z* 200. Thereafter, spectral data were transformed to image data and analyzed using ImageQuest v1.0.1 (Thermo Fisher Scientific).

### Mechanical testing

Molars were isolated immediately after animals were euthanized. A compression test was conducted using a mechanical testing machine (Model TK-252C; Muromachi Kikai Co.). A load was placed at the center of the molar at a rate of 2 mm/min until the molar broke, and maximum load (N) was measured as tooth strength.

### scRNA-seq

Dental pulps were collected and incubated for 30 min at 37°C in DMEM containing 1% collagenase D (from *C. histolyticum*; C5138-1G; Sigma-Aldrich), 1 U/ml dispase (17105-041; Thermo Fisher Scientific), and 1 U/ml DNase (Invitrogen) before cells were dissociated by trituration. The cells were dissociated to generate a single-cell suspension by filtering thorough a 40-µm nylon mesh. Cells were stained with propidium iodide (421301; 1:500; BioLegend). Propidium iodide–negative cells were sorted with a Cell Sorter SH800Z (Sony). Single cells were captured using a Chromium instrument (10x Genomics). Libraries were constructed using a commercial microdroplet-based platform, Chromium Single Cell 3′ v3.1 (10x Genomics) according to the manufacturer's instructions. A DNBSEQ-G400 platform (MGI) was used to sequence 28 and 91 base paired-end reads. Sequenced reads were aligned to the reference genome (mm10) using Cell Ranger v6.0.1 software (10x Genomics). The data were processed and analyzed using Seurat package v4.0.1. UMAP was used for the dimensionality reduction that captured both the local and global structure in scRNA-seq data. Clusters identified by *k*-means clustering analysis were visualized in 2 dimensions as feature or violin plots and annotated based on expression of canonical cell-type markers. Differentially expressed genes were extracted using the Wilcoxon rank sum test in the Seurat package. Gene expression was averaged in each cluster, and the correlation matrix was calculated by Pearson correlations. GO analysis of upregulated genes in control cells (log fold-change [FC] > 0.25) and *Vegfr2*$^{i\Delta EC}$ cells (log FC > 0.3) was conducted using the Database for Annotation, Visualisation, and Integrated Discovery (DAVID). Heatmaps showed the z-scores of average UMI counts in each cluster, visualized by the seaborn v0.11.0 package. Single-cell gene expression profiles from each cluster identified by scRNA-seq were further analyzed using CellPhoneDB (Efremova et al., 2020).

### Statistics

Results are expressed as means ± SD. Comparisons between two groups were evaluated using a two-tailed Student's *t* test.

Comparisons between multiple groups were evaluated using two-way ANOVA followed by Bonferroni's multiple comparison test. P values <0.05 were considered statistically significant.

### Online supplemental material

Fig. S1 shows immunohistological and qPCR data for the temporal transition of Vegf receptor expression in teeth. Fig. S2 shows the phenotype of *Vegfr2*$^{i\Delta EC}$ mice in the delayed deletion protocol. Fig. S3 shows the phenotype of *Osx-Cre*$^{ERT2+}$*Vegfr2*$^{flox/flox}$ mice characterized by no apparent blood vessel or odontoblast defects. Fig. S4 shows the data for quality control and additional information for cell type annotation in scRNA-seq. Video 1 shows a 3D reconstructed video of immunohistochemistry on the first molar at P12 showing that POTCs perforate the basal layer of odontoblasts. Table S1 shows raw data for metabolome analysis. Table S2 lists the top 100 enriched genes for each cluster in scRNA-seq analysis. Table S3 lists differentially expressed genes in control and *Vegfr2*$^{i\Delta EC}$ mice. Table S4 lists differentially expressed genes in odontoblast clusters (OB1, OB2, OB3) of control and *Vegfr2*$^{i\Delta EC}$ mice. Table S5 lists differentially expressed genes in endothelial clusters (EC1, EC2) of control and *Vegfr2*$^{i\Delta EC}$ mice.

## Data availability

Raw scRNA-seq data is available in GEO (GSE181175). There is no restriction on data availability.

## Acknowledgments

We thank Prof. Henry M. Kronenberg (Harvard University, Cambridge, MA) for kindly providing *Osx-Cre*$^{ERT2}$ mice.

This work was supported by Grants-in-Aid for Specially Promoted Research from the Ministry of Education, Culture, Sports, Science, and Technology of Japan (18H05042, 18K19553, and 19H03397); by Japan Agency for Medical Research and Development–PRIME (AMED-PRIME; JP20gm6210017h0002 and 21gm6210017h0003); by Japan Science and Technology Agency (MoonshotR&D; JPMJMS 2024); and by research grants from the following: Inamori Foundation, Kao Foundation for Arts and Culture, Takeda Science Foundation, Mochida Memorial Foundation, Mitsubishi Foundation, Cell Science Research Foundation, SENSHIN Medical Research Foundation, Sumitomo Foundation, Daiichi Sankyo Foundation of Life Science, Naito Foundation, Uehara Memorial Foundation, and Toray Science Foundation.

Author contributions: Designed experiments: Y. Kubota. Performed experiments: T. Matsubara, T. Iga, Y. Sugiura, T. Sanosaka, and I. Tai-Nagara. Analyzed data: T. Matsubara, Y. Sugiura, D. Kusumoto, T. Sanosaka, J. Kohyama, H. Okano, and M. Suematsu. Provided experimental materials: N. Takeda, G.-H. Fong, K. Ito, and M. Ema. Edited the manuscript: D. Kusumoto, T. Sanosaka, H. Okano, and M. Suematsu. Wrote the paper: Y. Kubota.

Disclosures: The authors declare no competing interests exist.

Submitted: 23 August 2021
Revised: 25 December 2021
Accepted: 17 February 2022

## References

Augustin, H.G., and G.Y Koh. 2017. Organotypic vasculature: From descriptive heterogeneity to functional pathophysiology. *Science*. 357:6353: eaal2379. https://doi.org/10.1126/science.aal2379

Biehs, B., J.K. Hu, N.B. Strauli, E. Sangiorgi, H. Jung, R.P. Heber, S. Ho, A.F. Goodwin, J.S. Dasen, M.R. Capecchi, and O.D Klein. 2013. BMI1 represses Ink4a/Arf and Hox genes to regulate stem cells in the rodent incisor. *Nat. Cell Biol.* 15:846–852. https://doi.org/10.1038/ncb2766

del Toro, R., C. Prahst, T. Mathivet, G. Siegfried, J.S. Kaminker, B. Larrivee, C. Breant, A. Duarte, N. Takakura, A. Fukamizu, et al. 2010. Identification and functional analysis of endothelial tip cell-enriched genes. *Blood*. 116: 4025–4033. https://doi.org/10.1182/blood-2010b02-270819

Duan, X., Y. Murata, Y. Liu, C. Nicolae, B.R. Olsen, and A.D. Berendsen. 2015. Vegfa regulates perichondrial vascularity and osteoblast differentiation in bone development. *Development*. 142:1984–1991. https://doi.org/10.1242/dev.117952

Efremova, M., M. Vento-Tormo, S.A. Teichmann, and R. Vento-Tormo. 2020. CellPhoneDB: Inferring cell–cell communication from combined expression of multi-subunit ligand-receptor complexes. *Nat. Protoc.* 15: 1484–1506. https://doi.org/10.1038/s41596-020s4150292-x

Gerber, H.P., T.H. Vu, A.M. Ryan, J. Kowalski, Z. Werb, and N. Ferrara. 1999. VEGF couples hypertrophic cartilage remodeling, ossification and angiogenesis during endochondral bone formation. *Nat. Med.* 5:623–628. https://doi.org/10.1038/9467

Gerhardt, H., M. Golding, M. Fruttiger, C. Ruhrberg, A. Lundkvist, A. Abramsson, M. Jeltsch, C. Mitchell, K. Alitalo, D. Shima, and C. Betsholtz. 2003. VEGF guides angiogenic sprouting utilizing endothelial tip cell filopodia. *J. Cell Biol.* 161:1163–1177. https://doi.org/10.1083/jcb.200302047

Ho, V.C., L.J. Duan, C. Cronin, B.T. Liang, and G.H. Fong. 2012. Elevated vascular endothelial growth factor receptor-2 abundance contributes to increased angiogenesis in vascular endothelial growth factor receptor-1-deficient mice. *Circulation*. 126:741–752. https://doi.org/10.1161/CIRCULATIONAHA.112.091603

Hooper, A.T., J.M. Butler, D.J. Nolan, A. Kranz, K. Iida, M. Kobayashi, H.G. Kopp, K. Shido, I. Petit, K. Yanger, et al. 2009. Engraftment and reconstitution of hematopoiesis is dependent on VEGFR2-mediated regeneration of sinusoidal endothelial cells. *Cell Stem Cell*. 4:263–274. https://doi.org/10.1016/j.stem.2009.01.006

Hu, S., J. Wang, E.H. Ji, T. Christison, L. Lopez, and Y. Huang. 2015. Targeted metabolomic analysis of head and neck cancer cells using high performance ion chromatography coupled with a Q exactive HF mass spectrometer. *Anal. Chem.* 87:6371–6379. https://doi.org/10.1021/acs.analchem.5b01350

Hu, K., and B.R. Olsen. 2016. Osteoblast-derived VEGF regulates osteoblast differentiation and bone formation during bone repair. *J. Clin. Invest.* 126:509–526. https://doi.org/10.1172/JCI82585

Ishitobi, H., K. Matsumoto, T. Azami, F. Itoh, S. Itoh, S. Takahashi, and M. Ema. 2010. Flk1-GFP BAC Tg mice: An animal model for the study of blood vessel development. *Exp. Anim.* 59:615–622. https://doi.org/10.1538/expanim.59.615

Jin, L., F. Gao, L. Zhang, C. Wang, L. Hu, Z. Fan, and D. Xia. 2021. Pleiotropin enhances the osteo/dentinogenic differentiation potential of dental pulp stem cells. *Connect. Tissue Res.* 62:495–507. https://doi.org/10.1080/03008207.2020.1779238

Kaukua, N., M.K. Shahidi, C. Konstantinidou, V. Dyachuk, M. Kaucka, A. Furlan, Z. An, L. Wang, I. Hultman, L. Ahrlund-Richter, et al. 2014. Glial origin of mesenchymal stem cells in a tooth model system. *Nature*. 513: 551–554. https://doi.org/10.1038/nature13536

Kalucka, J., L.P.M.H. de Rooij, J. Goveia, K. Rohlenova, S.J. Dumas, E. Meta, N.V. Conchinha, F. Taverna, L.A. Teuwen, K. Veys, et al. 2020. Single-cell transcriptome atlas of murine endothelial cells. *Cell*. 180:764–779.e20. https://doi.org/10.1016/j.cell.2020.01.015

Kawamoto, S., H. Niwa, F. Tashiro, S. Sano, G. Kondoh, J. Takeda, K. Tabayashi, and J. Miyazaki. 2000. A novel reporter mouse strain that expresses enhanced green fluorescent protein upon Cre-mediated recombination. *FEBS Lett.* 470:263–268. https://doi.org/10.1016/s0014-5793(00)01338-7

Kubota, Y., K. Takubo, M. Hirashima, N. Nagoshi, K. Kishi, Y. Okuno, A. Nakamura-Ishizu, K. Sano, M. Murakami, M. Ema, et al. 2011. Isolation and function of mouse tissue resident vascular precursors marked by myelin protein zero. *J. Exp. Med.* 208:949–960. https://doi.org/10.1084/jem.20102187

Kubota, Y., M. Hirashima, K. Kishi, C. L. Stewart, and T. Suda. 2008. Leukemia inhibitory factor regulates microvessel density by modulating

oxygen-dependent VEGF expression in mice. *J. Clin. Invest.* 118:2393–2403. https://doi.org/10.1172/JCI34882

Kusumbe, A.P., S.K. Ramasamy, A. Starsichova, and R.H. Adams. 2015. Sample preparation for high-resolution 3D confocal imaging of mouse skeletal tissue. *Nat. Protoc.* 10:1904–1914. https://doi.org/10.1038/nprot.2015.125

Kusumbe, A.P., S.K. Ramasamy, and R.H. Adams. 2014. Coupling of angiogenesis and osteogenesis by a specific vessel subtype in bone. *Nature.* 507:323–328. https://doi.org/10.1038/nature13145

Lendahl, U., L.B. Zimmerman, and R.D. McKay. 1990. CNS stem cells express a new class of intermediate filament protein. *Cell.* 60:585–595. https://doi.org/10.1016/0092-8674(90)90662-x

Li, J., J. Feng, Y. Liu, T.V. Ho, W. Grimes, H.A. Ho, S. Park, S. Wang, and Y. Chai. 2015. BMP-SHH signaling network controls epithelial stem cell fate via regulation of its niche in the developing tooth. *Dev. Cell.* 33:125–135. https://doi.org/10.1016/j.devcel.2015.02.021

Li, J., C. Parada, and Y. Chai. 2017. Cellular and molecular mechanisms of tooth root development. *Development.* 144:374–384. https://doi.org/10.1242/dev.137216

Maes, C., T. Kobayashi, M.K. Selig, S. Torrekens, S.I. Roth, S. Mackem, G. Carmeliet, and H.M. Kronenberg. 2010. Osteoblast precursors, but not mature osteoblasts, move into developing and fractured bones along with invading blood vessels. *Dev. Cell.* 19:329–344. https://doi.org/10.1016/j.devcel.2010.07.010

Maes, C., and T.L. Clemens. 2014. Angiogenic–osteogenic coupling: The endothelial perspective. *Bonekey Rep.* 3:578. https://doi.org/10.1038/bonekey.2014.73

Melin, M., A. Joffre-Romeas, J.C. Farges, M.L. Couble, H. Magloire, and F. Bleicher. 2000. Effects of TGFbeta1 on dental pulp cells in cultured human tooth slices. *J. Dent Res.* 79:1689–1696. https://doi.org/10.1177/00220345000790090901

Morita, M., T. Sato, M. Nomura, Y. Sakamoto, Y. Inoue, R. Tanaka, S. Ito, K. Kurosawa, K. Yamaguchi, Y. Sugiura, et al. 2018. PKM1 confers metabolic advantages and promotes cell-autonomous tumor cell growth. *Cancer Cell.* 33:355–367.e7. https://doi.org/10.1016/j.ccell.2018.02.004

Ono, W., N. Sakagami, S. Nishimori, N. Ono, and H.M. Kronenberg. 2016. Parathyroid hormone receptor signalling in osterix-expressing mesenchymal progenitors is essential for tooth root formation. *Nat. Commun.* 7:11277. https://doi.org/10.1038/ncomms11277

Okabe, K., S. Kobayashi, T. Yamada, T. Kurihara, I. Tai-Nagara, T. Miyamoto, Y.S. Mukouyama, T.N. Sato, T. Suda, M. Ema, and Y. Kubota. 2014. Neurons limit angiogenesis by titrating VEGF in retina. *Cell.* 159:584–596. https://doi.org/10.1016/j.cell.2014.09.025

Pagella, P., L. de Vargas Roditi, B. Stadlinger, A.E. Moor, and T.A. Mitsiadis. 2021. A single-cell atlas of human teeth. *iScience.* 24:102405. https://doi.org/10.1016/j.isci.2021.102405

Potente, M., H. Gerhardt, and P. Carmeliet. 2011. Basic and therapeutic aspects of angiogenesis. *Cell.* 146:873–887. https://doi.org/10.1016/j.cell.2011.08.039

Rafii, S., J.M. Butler, and B.S. Ding. 2016. Angiocrine functions of organ-specific endothelial cells. *Nature.* 529:316–325. https://doi.org/10.1038/nature17040

Rombouts, C., T. Giraud, C. Jeanneau, and I. About. 2017. Pulp vascularization during tooth development, regeneration, and therapy. *J. Dent. Res.* 96:137–144. https://doi.org/10.1177/0022034516671688

Simmer, J.P., P. Papagerakis, C.E. Smith, D. C. Fisher, A.N. Rountrey, L. Zheng, and J.C. Hu. 2010. Regulation of dental enamel shape and hardness. *J. Dent. Res.* 89:1024–1038. https://doi.org/10.1177/0022034510375829

Sivaraj, K.K., and R.H. Adams. 2016. Blood vessel formation and function in bone. *Development.* 143:2706–2715. https://doi.org/10.1242/dev.136861

Sugiura, Y., K. Honda, M. Kajimura, and M. Suematsu. 2014. Visualization and quantification of cerebral metabolic fluxes of glucose in awake mice. *Proteomics.* 14:829–838. https://doi.org/10.1002/pmic.201300047

Sugiura, Y., Y. Katsumata, M. Sano, K. Honda, M. Kajimura, K. Fukuda, and M. Suematsu. 2016. Visualization of in vivo metabolic flows reveals accelerated utilization of glucose and lactate in penumbra of ischemic heart. *Sci. Rep.* 6:32361. https://doi.org/10.1038/srep32361

Tai-Nagara, I., Y. Hasumi, D. Kusumoto, H. Hasumi, K. Okabe, T. Ando, F. Matsuzaki, F. Itoh, H. Saya, C. Liu, et al. 2020. Blood and lymphatic systems are segregated by the FLCN tumor suppressor. *Nat. Commun.* 11:6314. https://doi.org/10.1038/s41467-020

Thesleff, I., and P. Sharpe. 1997. Signalling networks regulating dental development. *Mech. Dev.* 67:111–123. https://doi.org/10.1016/s0925-4773(97)00115-9

Tucker, A., and P. Sharpe. 2004. The cutting-edge of mammalian development; how the embryo makes teeth. *Nat. Rev. Genet.* 5:499–508. https://doi.org/10.1038/nrg1380

Tummers, M., and I. Thesleff. 2003. Root or crown: A developmental choice orchestrated by the differential regulation of the epithelial stem cell niche in the tooth of two rodent species. *Development.* 130:1049–1057. https://doi.org/10.1242/dev.00332

Vanlandewijck, M., L. He, M.A. Mäe, J. Andrae, K. Ando, F. Del Gaudio, K. Nahar, T. Lebouvier, B. Laviña, L. Gouveia, et al. 2018. A molecular atlas of cell types and zonation in the brain vasculature. *Nature.* 554:475–480. https://doi.org/10.1038/nature25739

Wang, Y., C. Wan, L. Deng, X. Liu, X. Cao, S. R. Gilbert, M.L. Bouxsein, M.C. Faugere, R.E. Guldberg, L.C. Gerstenfeld, et al. 2007. The hypoxia-inducible factor alpha pathway couples angiogenesis to osteogenesis during skeletal development. *J. Clin. Invest.* 117:1616–1626. https://doi.org/10.1172/JCI31581

West, H., W.D. Richardson, and M. Fruttiger. 2005. Stabilization of the retinal vascular network by reciprocal feedback between blood vessels and astrocytes. *Development.* 132:1855–1862. https://doi.org/10.1242/dev.01732

Yamamoto, T., N. Takano, K. Ishiwata, M. Ohmura, Y. Nagahata, T. Matsuura, A. Kamata, K. Sakamoto, T. Nakanishi, A. Kubo, et al. 2014. Reduced methylation of PFKFB3 in cancer cells shunts glucose towards the pentose phosphate pathway. *Nat. Commun.* 5:3480. https://doi.org/10.1038/ncomms4480

## Supplemental material

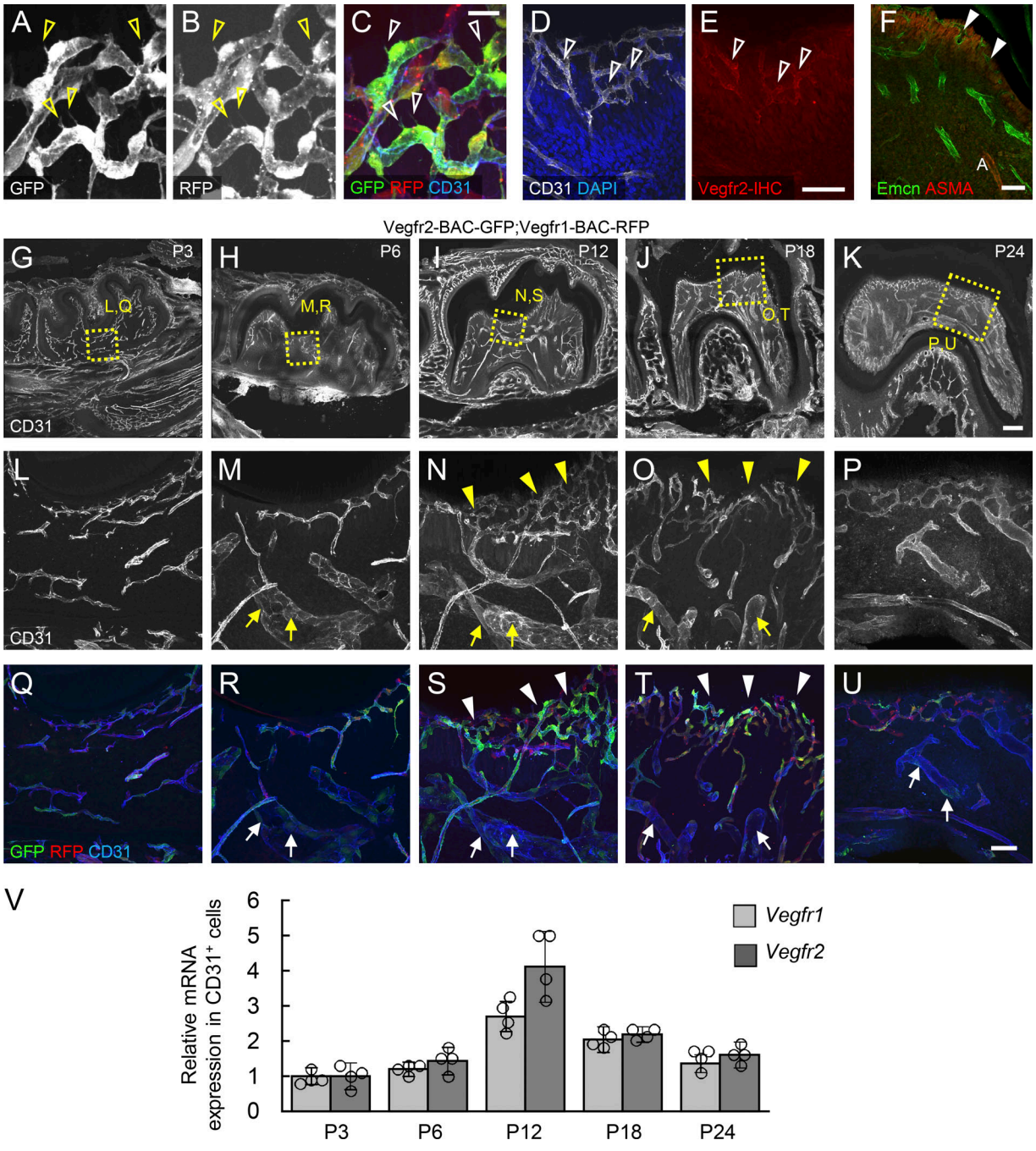


Figure S1. **Temporal transition of Vegf receptor expression in teeth. (A–F)** Immunohistochemistry of a mandible centered on the first molar. Vegfr1$^{high}$ and Vegfr2$^{high}$ ECs are actively sprouting (open arrowheads) and lack smooth muscle cells (closed arrowheads). ASMA, α-smooth muscle actin. **(A–C)** These images show separate channels of Fig. 1 I. **(D)** Fig. 1 D shows the same image for the sake of convenience. **(G–U)** Immunohistochemistry for mandibles centered on the first molar. Looping venules (arrows) were clearly detected after P6, while Vegfr1$^{high}$Vegfr2$^{high}$ POTCs (closed arrowheads) developed at ∼P12. **(V)** qPCR analysis of isolated CD31$^{+}$ dental pulp cells ($n$ = 4 respectively). Scale bars: 200 µm (G–K); 50 µm (D–F and L–U); 20 µm (A–C). Data are presented as means ± SD.

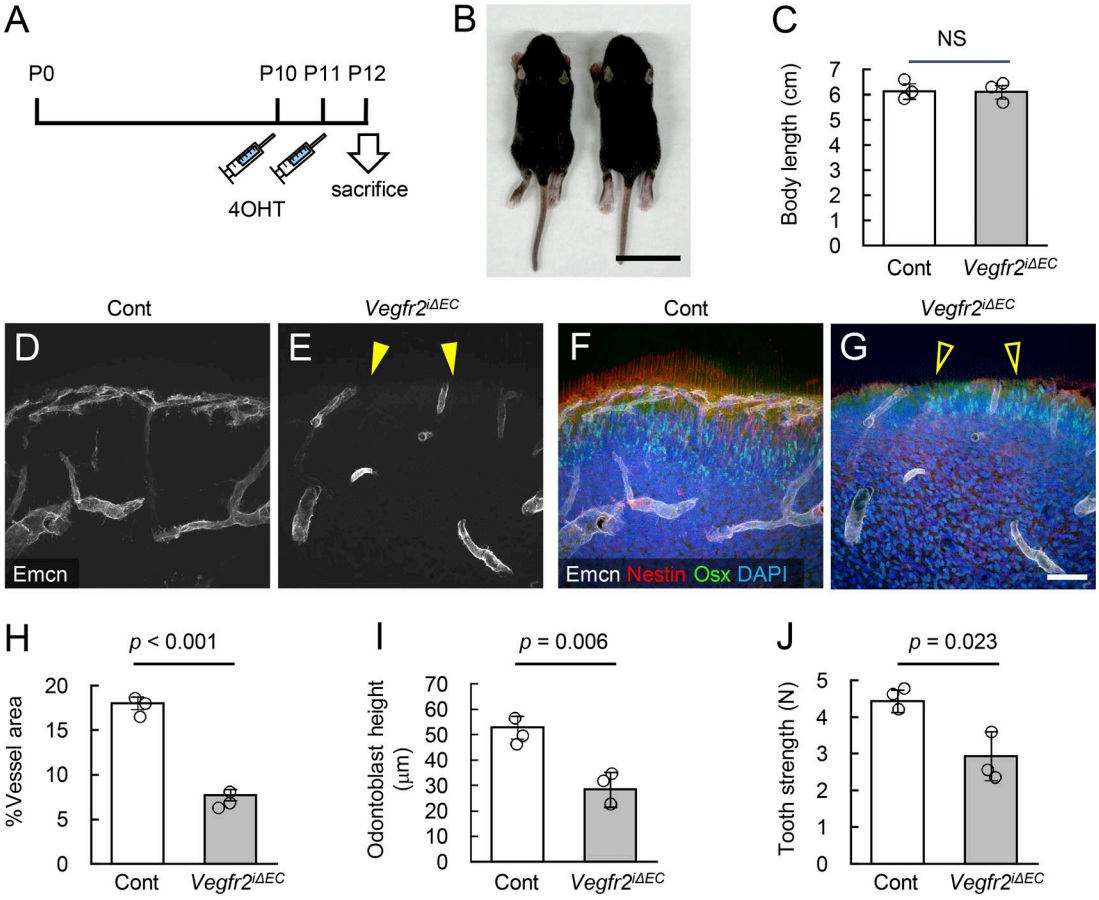


Figure S2. **Delayed Vegfr2 deletion impairs vessel invasion and odontoblast maturation. (A)** Protocol for 4OHT injection. **(B and C)** Gross appearance and quantification of body length of mice at P12 (control [Cont] $n = 3$, *Vegfr2*$^{i\Delta EC}$ $n = 3$). **(D–I)** Immunohistochemistry of a mandible centered on the first molar and quantification (Cont $n = 3$, *Vegfr2*$^{i\Delta EC}$ $n = 3$). **(J)** Tooth mechanical strength measured by a compression test (Cont $n = 3$, *Vegfr2*$^{i\Delta EC}$ $n = 3$). Scale bars: 2 cm (B); 50 μm (D–G). Data are presented as means ± SD. Comparisons between two groups were evaluated using a two-sided Student's *t* test.

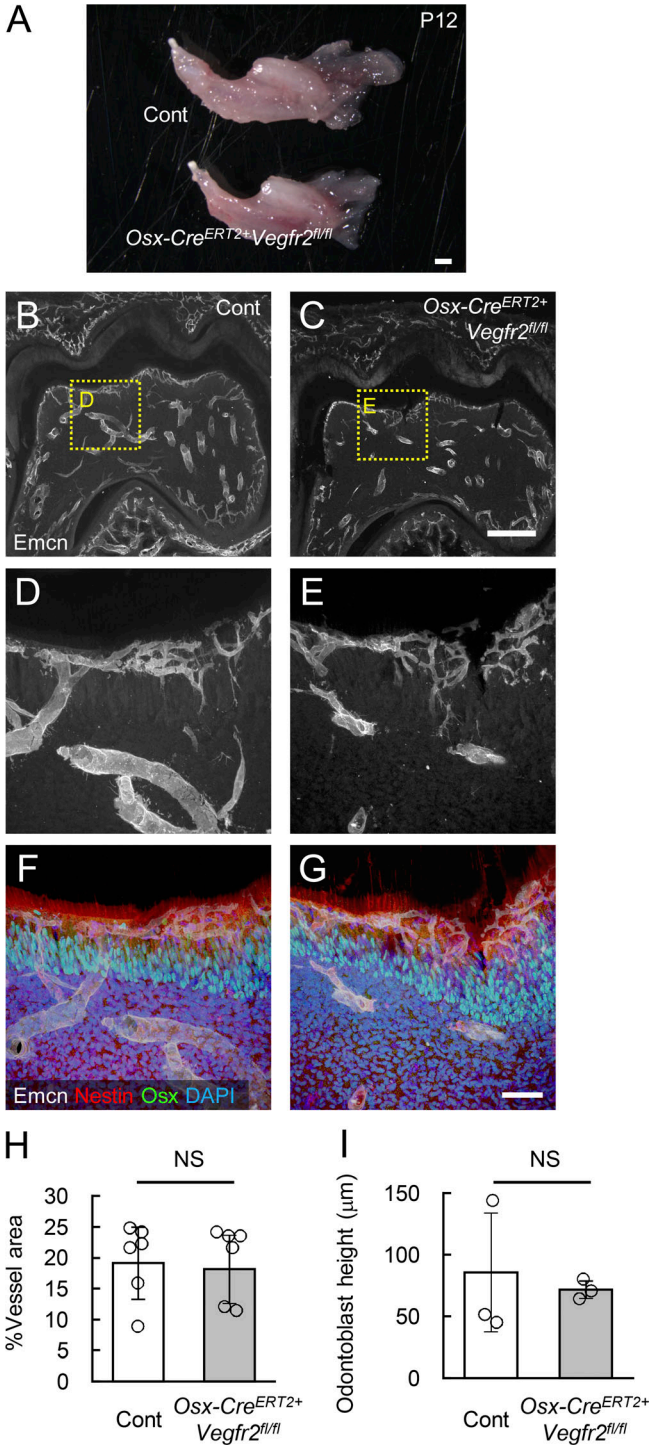


Figure S3. **Odontoblast Vegfr2 was dispensable for tooth formation. (A)** Bright-field view of mandibles. Molar extrusion was intact in *Osx–Cre*$^{ERT2+}$*Vegfr2*$^{flox/flox}$ mice. **(B–I)** Section specimens at P12 and quantification (H, control [Cont] $n$ = 6, *Osx–Cre*$^{ERT2+}$*Vegfr2*$^{flox/flox}$ $n$ = 6; I, Cont $n$ = 3, *Osx–Cre*$^{ERT2+}$*Vegfr2*$^{flox/flox}$ $n$ = 3). *Osx–Cre*$^{ERT2+}$*Vegfr2*$^{flox/flox}$ mice exhibited no apparent blood vessel or odontoblast defects. Scale bars: 500 µm (A); 200 µm (B and C); 50 µm (D–G). Data are presented as means ± SD. Comparisons between two groups were evaluated using a two-sided Student's $t$ test.

A

| | Control | *Vegfr2*$^{i\Delta EC}$ |
|---|---|---|
| Estimated Number of Cells | 3,487 | 2563 |
| Mean Reads per cell | 91497 | 103106 |
| Median Gene per cell | 2953 | 2213 |
| Valid Barcodes | 95.6% | 96.6% |
| Sequencing Saturation | 70.06% | 82.5% |
| Q30 Bases in Barcode | 87.1% | 86.1% |
| Q30 Bases in RNA Read | 85.6% | 84.5% |
| Q30 Bases in UMI | 85.3% | 83.8% |
| Reads Mapped Confidently to Transcriptome | 55.1% | 53.3% |
| Reads Mapped Confidently to Exonic Regions | 58.9% | 56.7% |
| Reads Mapped Confidently to Intronic Regions | 27.3% | 30.7% |
| Reads Mapped Confidently to Intergenic Regions | 5.6% | 6.9% |

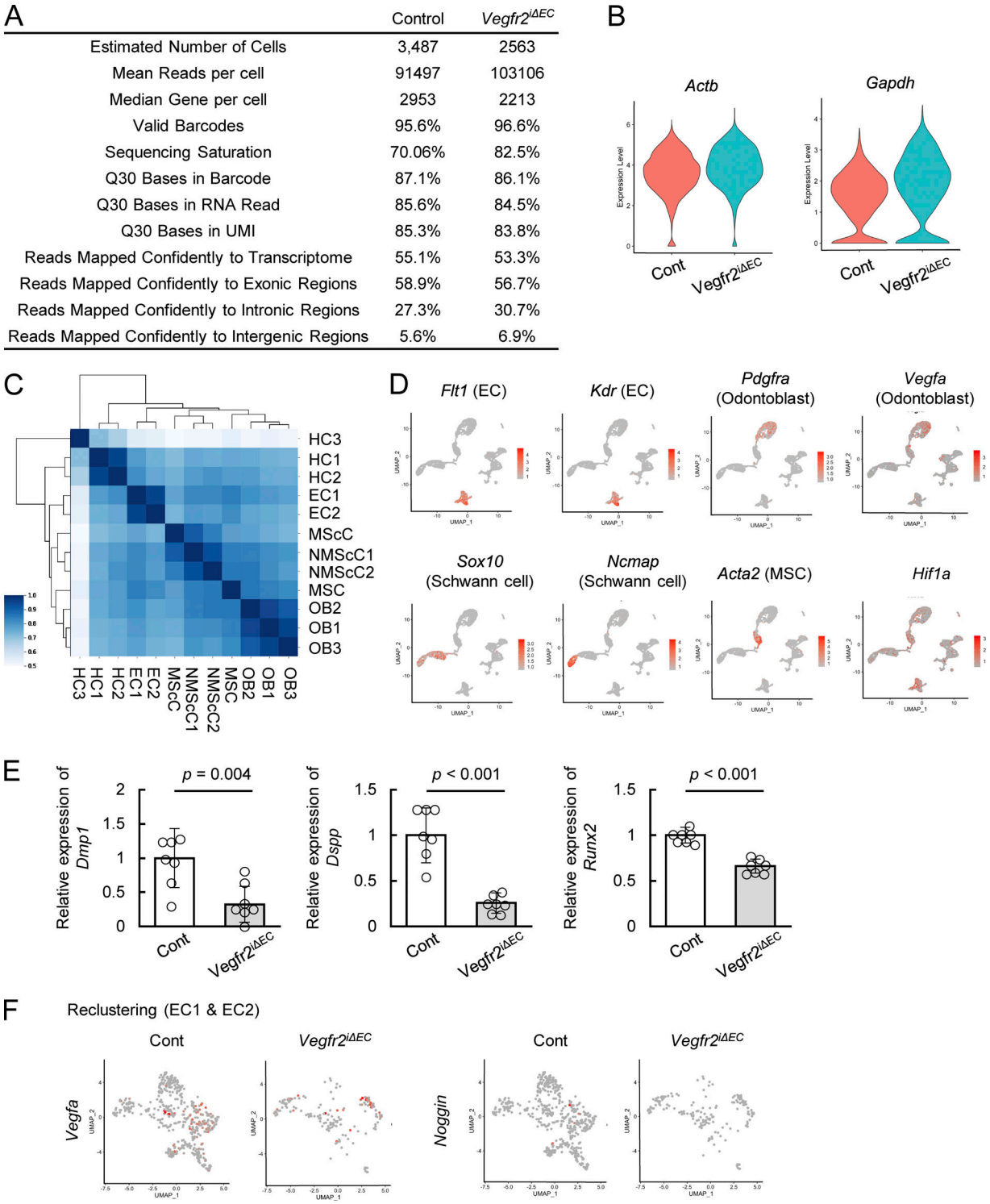


Figure S4. **Quality control and characterization of cells in scRNA-seq. (A)** Statistics of cells analyzed in scRNA-seq. **(B)** Violin plots for internal control genes used the comparison of cells from control and *Vegfr2*$^{i\Delta EC}$ mice. **(C)** Pearson correlation matrix of the average expression profiles of all subpopulations based on all differentially expressed genes. **(D)** UMAP plots showing marker genes. **(E)** qPCR analysis of freshly isolated dental pulp cells at P12 (control [Cont] $n = 7$, *Vegfr2*$^{i\Delta EC}$ $n = 7$), confirming the scRNA-seq results. **(F)** UMAP plots showing expression of *Vegfa* and *Noggin* in reclustered EC1 and EC2 cells in Fig. 7 B. Data are presented as means ± SD. Comparisons between two groups were evaluated using a two-sided Student's *t* test.

Video 1. **Spatial relationship between POTCs and odontoblasts.** 3D reconstructed video showing immunohistochemistry on the first molar at P12 stained by Endomucin (white), Osx (green), and Nestin (red). POTCs perforated the basal layer of odontoblasts, marked by Osx.

**Provided online are Table S1, Table S2, Table S3, Table S4, and Table S5. Table S1 lists raw data for metabolome analysis. Table S2 lists the top 100 enriched genes for each cluster in scRNA-seq analysis. Table S3 lists differentially expressed genes in *Vegfr2*$^{i\Delta EC}$ mice. Table S4 lists differentially expressed genes in odontoblast clusters (OB1, OB2, OB3) of *Vegfr2*$^{i\Delta EC}$ mice. Table S5 lists differentially expressed genes in endothelial clusters (EC1, EC2) of *Vegfr2*$^{i\Delta EC}$ mice.**